Elsevier Editorial System(tm) for Deep-Sea Research Part I

Manuscript Draft

Manuscript Number: DSR1-D-06-00128R1

Title: Internal Tide Generation by Seamounts

Article Type: Regular Manuscript

Keywords: Internal tides; internal waves; seamounts; tidal dissipation

Corresponding Author: Dr. Peter George Baines, PhD

Corresponding Author's Institution: University of Melbourne

First Author: Peter George Baines, PhD

Order of Authors: Peter George Baines, PhD

Abstract: The generation of internal tidal wave fields by barotropic tidal flow past a representative seamount are computed by modelling the seamount as a pillbox, and linearising the equations for internal wave dynamics. This is justifiable for mid-ocean seamounts, which constitute steep topography for internal waves of tidal frequency. For linearly polarized barotropic tidal flow, the resulting flow field consists of conical beams radiating from the region above the seamount, with largest velocities aligned with the barotropic flow. These beams vary with azimuthal angle but resemble the corresponding beams from two-dimensional steep topography, particularly in the barotropic flow direction. They are primarily forced by the barotropic flow over the seamount, which is amplified by the topography and is independent of the stratification if the radius of the seamount is sufficiently large. In a barotropic tidal flow of 1 cm/sec amplitude, energy fluxes from individual seamounts are of order 106 Watt. Summing this over all seamounts higher than 1 km gives baroclinic energy generation of order 5.109 Watt, a number that is less than estimates of baroclinic energy flux from the continental slopes and the Hawaiian ridge, but is comparable with them.

Internal Tide Generation by Seamounts

Peter G. Baines

Dept. of Civil and Environmental Engineering,
University of Melbourne, Melbourne, Australia 3010 and
QUEST, Dept. of Earth Sciences, Bristol BS8 1RJ, UK

Abstract

The generation of internal tidal wave fields by barotropic tidal flow past a representative seamount are computed by modelling the seamount as a pillbox, and linearising the equations for internal wave dynamics. This is justifiable for mid-ocean seamounts, which constitute steep topography for internal waves of tidal frequency. For linearly polarized barotropic tidal flow, the resulting flow field consists of conical beams radiating from the region above the seamount, with largest velocities aligned with the barotropic flow. These beams vary with azimuthal angle but resemble the corresponding beams from two-dimensional steep topography, particularly in the barotropic flow direction. They are primarily forced by the barotropic flow over the seamount, which is amplified by the topography and is independent of the stratification if the radius of the seamount is sufficiently large. In a barotropic tidal flow of 1 cm/sec amplitude, energy fluxes from individual seamounts are of order 10^6 Watt. Summing this over all seamounts higher than 1 km gives baroclinic energy generation of order 5.10^9 Watt, a number that is less

than estimates of baroclinic energy flux from the continental slopes and the Hawaiian ridge, but is comparable with them.

1. Introduction

The generation of internal tides in the deep ocean is of considerable current interest for several reasons, as follows. Recent observations have shown them to have larger amplitudes than previously expected (Morozov 1995), most notably near the Hawaiian ridge (Ray & Mitchum 1997, Rudnick et al. 2003). Further, in conjunction with the presence of topography, they are thought to be important in providing an energy source for vertical mixing in the deep ocean (Munk and Wunsch 1998). Internal tides are generated by the tidal flow of the density-stratified ocean over bottom topography, and the first stage in understanding their effects is to understand and be able to calculate this generation process. To date, most theoretical studies have focused on generation from two-dimensional topography, and for decades much attention has been focused on generation from coastal topography, beginning with Rattray (1960). The relatively small number of studies of generation by three-dimensional topography have been with linearised bottom topography (Bell 1975, Llewellyn Smith and Young 2002) or numerical models (Holloway and Merrifield 1999, Munroe and Lamb 2005). A recent review of the field is given by Garrett and Kunze (2007).

For topography of finite height, the mathematical problem is very different depending on whether the topography is “flat”, in which the slope of the rays (group velocity vectors) of the internal tide is always steeper than the topography that they encounter (Baines

1973), or “steep”, where the topography is steeper in some locations (e.g. Baines 1974). In the latter case, the problem can be sometimes simplified by assuming that the topography has vertical sides. If one wishes to apply such a model to topography with non-vertical sides, the solution obtained should have small amplitude in the region of difference, and this constitutes a check on this approximation. In the case of two-dimensional topography, it is seen to work quite well (Prinsenberg and Rattray 1975).. The non-horizontal terms of the Coriolis force may also be included in linear models (Baines and Miles 2000); these cause changes to the locations of the rays, but the extra complexity is not justified for present purposes and they are not included here.

This paper presents a study of baroclinic tidal generation for steep-sided axisymmetric topography that approximates typical seamounts. The equations are linearised, and the seamount is assumed to have a flat top or summit, with vertical sides or flanks. In spite of these approximations, this model is believed to provide a good description of the overall properties of the flow, and to give a soundly based estimate of the energy fluxes produced. The model and mathematical details are described in section 2, and the results for individual seamounts are presented in section 3. This includes a description of the flow over and around the seamount, the dependence of the energy flux on the relevant dimensionless parameters, and results for different upper level stratification. In section 4, these results are used to integrate the energy flux over (model representations of) the whole seamount population in the deep ocean. These results are compared with calculations by others (Llewellyn Smith & Young 2002, 2003 and St. Laurent et al. 2003) for linearised or two-dimensional topography in section 5, and the conclusions are summarized and discussed in section 6.

2. The model and equations

Seamounts are small topographic features in the ocean compared with the scale of ocean basins, and with the scale of variations of the barotropic tide. Horizontal scales are generally less than 100 km. Accordingly, within the vicinity of an individual seamount situated on an otherwise flat ocean floor, the background barotropic tide may be assumed to be spatially uniform. Barotropic tidal motion generally has the form of an ellipse for the velocity vectors and the particle displacement, for each tidal component. This may be represented as the sum of two rectilinear motions at right angles. If the resulting baroclinic motions are small enough to be regarded as linear, the response to the elliptic barotropic tide may be represented as the sum of the responses to these two rectilinear motions. Hence, it suffices to consider the baroclinic generation from a single rectilinear barotropic tidal motion, and sum the results from the two orthogonal constituents to obtain the nett results for forcing by the elliptical motion.

One conceptual approach to internal tide generation is to first obtain the flow pattern that would exist if the ocean were unstratified, which could be termed the virtual barotropic flow. The advection of density surfaces by this flow constitutes the forcing for the baroclinic tide (Baines 1973). In the case of a non-rotating ocean, small-amplitude periodic flow past a seamount has the form of three-dimensional potential flow in homogeneous fluid of finite depth. In a rotating homogeneous ocean in which potential vorticity is conserved, the situation is more complex, and is unattractive as a computational procedure. A better way of obtaining the internal tide is to consider the full stratified problem in which only the background barotropic flow is specified. The barotropic flow over and in the vicinity of the seamount is then determined as part of the solution, and is dependent on the stratification, as seen below.

We therefore assume that the background barotropic velocity $\boldsymbol{u}_b$ has the form

$$\boldsymbol{u}_b = U\hat{\boldsymbol{x}}\, cos\, \omega t\,, \tag{2.1}$$

where U is the amplitude of the rectilinear motion, ω is the tidal frequency, and $\hat{\boldsymbol{x}}$ is the unit vector in the x-direction. The equations for the motion of an incompressible density-stratified ocean, assuming that these are small enough to be linear, are

$$\frac{\partial \boldsymbol{u}}{\partial t} + \boldsymbol{f}x\boldsymbol{u} = -\frac{1}{\rho_0}\nabla p - \frac{g\rho'}{\rho_0}\ , \tag{2.2}$$

$$\frac{\partial \rho'}{\partial t} + w\frac{\mathrm{d}\rho_0}{\mathrm{d}z} = 0\,, \qquad \nabla.\boldsymbol{u} = 0\ , \tag{2.3}$$

where ρ' is the perturbation density with ρ_0 a mean density, p pressure, g gravity and $\boldsymbol{f} = 2\Omega$ sin(latitude) $\hat{\boldsymbol{z}}$, where Ω is the angular velocity of the rotation of the Earth. The virtual barotropic tide mentioned above is governed by these equations with the buoyancy term in (2.2) omitted. Here we consider plane polar coordinates (r, θ), where r is radial horizontal distance from an origin, and θ is angular distance from the positive direction of the x- axis. From (2.2) the pressure field for the unidirectional background barotropic flow (2.1) is then given by

$$p = p_b = \rho_0 \omega U r\left(i\cos\theta - \frac{f}{\omega}\sin\theta \right)\mathrm{e}^{-i\omega t}\ , \tag{2.4}$$

where the real part is taken.

For linearised baroclinic motion with pressure p and vertical velocity w and time dependence $e^{-i\omega t}$, equations (2.2-2.3) give

$$\nabla_h^2 w - \frac{\omega^2 - f^2}{N(z)^2 - \omega^2} w_{zz} = 0, \tag{2.5}$$

$$\nabla_h^2 p - \left(\omega^2 - f^2\right) \frac{\partial}{\partial z}\left(\frac{p_z}{N(z)^2 - \omega^2}\right) = 0\,, \tag{2.6}$$

where ∇_h^2 is the horizontal Laplacian, and $N(z)$ is the buoyancy frequency defined by

$$N(z)^2 = -\frac{g}{\rho_0}\frac{\mathrm{d}\rho_0}{\mathrm{d}z}\,. \tag{2.7a}$$

The slope of the rays, or group velocity vectors of internal waves of frequency ω in fluid with buoyancy frequency N is c, where

$$c^2 = \frac{\omega^2 - f^2}{N^2 - \omega^2}\,. \tag{2.7b}$$

Horizontal velocity components (u_r, u_θ) in the radial and θ-directions are then given by

$$u_r = \frac{1}{\rho_0\left(\omega^2 - f^2\right)}\left(-i\omega\frac{\partial p}{\partial r} + \frac{f}{r}\frac{\partial p}{\partial \theta}\right), \quad u_\theta = -\frac{1}{\rho_0\left(\omega^2 - f^2\right)}\left(f\frac{\partial p}{\partial r} + \frac{i\omega}{r}\frac{\partial p}{\partial \theta}\right), \tag{2.8}$$

and the vertical velocity by

$$w = \frac{1}{\rho_0}\frac{i\omega}{\left(N(z)^2 - \omega^2\right)}\frac{\partial p}{\partial z}\,. \tag{2.9}$$

We consider seamounts with axi-symmetric geometry, and take the coordinate origin at the centre of the seamount as shown in Figure 1. Each seamount is assumed to have the shape of a “pillbox” – axisymmetric with a flat top and vertical sides. This is justified because seamounts are generally steep (typical slope angle 17° - Wessel 2001) and are much steeper than the slope c of the rays, which are typically 3-6°. Hence they may be assumed to be axi-symmetric "steep topography" in the language of previous two-dimensional studies (e.g. Baines 1973, 1974). The region on the top of the seamount has small slope, and is adequately represented by a horizontal surface. The geometry of the rays for the internal tide, therefore, is well-represented by those for a pillbox, for a typical seamount. This assumption is assessed below when the solutions are obtained. The pillbox has radius a and height h_m above the horizontal ocean bottom, in an ocean of total depth D_e. The coordinate origin is taken at the centre of the seamount, at the ocean surface.

The mathematical problem for the internal tide then takes the following form. The total tidal velocity $\boldsymbol{u}$ is equal to

$$\boldsymbol{u} = \boldsymbol{u}_b + \boldsymbol{u}_i, \tag{2.10}$$

where the background barotropic flow $\boldsymbol{u}_b$ is horizontal and given by (2.1) and $\boldsymbol{u}_i$ denotes the forced response due to the seamount. $\boldsymbol{u}_i = (u_{ir}, u_{i\theta}, w)$ in polar coordinates, with the boundary conditions

$$\begin{aligned} w = 0, \quad \text{on} \quad & z = 0, \\ & z = -(D_e - h_m), \ 0 < r < a, \\ & z = -D_e, \quad r > a, \end{aligned} \tag{2.11}$$

and

$$u_r = 0, \ u_{ir} = -u_{br} \text{ on } \quad r = a, \ -D_e < z < -(D_e - h_m). \tag{2.12}$$

Note that $\boldsymbol{u}_i$ will contain a non-zero vertically averaged (barotropic) component, to be determined as part of the solution. We also require radiation conditions for the far field (i.e. large r) which imply that there is no incoming internal wave energy from infinity.

We obtain solutions in terms of the pressure, and write $p = p_b + p_i$. It is then convenient to write p_b from (2.4) in the form

$$p_b = \rho_0 U \omega a \frac{r}{a}\frac{i}{2}\left[\left(1+\frac{f}{\omega}\right)\mathrm{e}^{i\theta} + \left(1-\frac{f}{\omega}\right)\mathrm{e}^{-i\theta}\right]\mathrm{e}^{-i\omega t} \ , \qquad (2.13)$$

so that p_i may be expressed

$$p_i = \rho_0 U \omega a [p_p(r,z)\mathrm{e}^{i\theta} + p_m(r,z)\mathrm{e}^{-i\theta}]\mathrm{e}^{-i\omega t}, \qquad (2.14)$$

the subscripts p and m notionally denoting “plus” and “minus” the $i\theta$ exponent. The conditions on w then imply that

$$\frac{\partial p_p}{\partial z} = 0, \frac{\partial p_m}{\partial z} = 0, \quad \text{on} \quad z = 0,$$

$$\text{and on} \quad z = -(D_e - h_m), \ 0 < r < a, \qquad (2.15)$$

$$z = -D_e, \quad r > a,$$

and

$$\frac{\partial p_p}{\partial r} - \frac{f}{\omega a} p_p = -\frac{i\left(1-\dfrac{f^2}{\omega^2}\right)}{2a}, \qquad \text{on} \quad r = a, \ -D_e < z < -(D_e - h_m), \qquad (2.16)$$

and similarly for p_m with $(-f)$ replacing f. We will be considering different forms of the solution in the regions $r > a$, and $0 < r < a$ above the seamount, and the conditions of continuity of u_r and p imply that p_p and p_m and their derivatives must be continuous across $r = a$ in the range $-(D_e - h_m) < z < 0$. Hence p_p and p_m are calculated separately.

For the motion above the summit of the seamount, there are two possibilities. The first is to assume that the wave field there is essentially inviscid, and may be regarded as a sum of discrete modes that do not contain singularities at the origin. This is mathematically simple, but as will be seen, the accurate description of the flow requires many vertical modes (typically, about 100 or more), and for many of these modes, the wavelengths are very short if the depth of the top of the seamount is shallow. Consequently, dissipation is likely to be significant, and it seems doubtful that in practice all of these modes will be coherent over the whole seamount summit, particularly if the seamount is not exactly circular. A more realistic option may be to assume that the baroclinic motion over the seamount is generated at the seamount edge, propagates inward and is dissipated without significant internal reflection occurring from the summit rim. Both of these cases are computed here. The real situation for a given seamount may be a mixture of the two – a small number of modes (one or two?) may have little dissipation and have standing – wave character over the seamount, with the rest having inward energy propagation from the outer edge, or summit rim, that is dissipated before reaching the far side.

From (2.6), both p_p and p_m satisfy

$$\frac{1}{r}\frac{\partial}{\partial r}\left(r\frac{\partial p_p}{\partial r}\right)-\frac{p_p}{r^2}-\left(\omega^2-f^2\right)\frac{\partial}{\partial z}\left(\frac{p_{p\,z}}{N(z)^2-\omega^2}\right)=0\,. \qquad (2.17)$$

This may be solved by separation of variables: $p_p = R(r)Z(z)$, giving

$$R_{rr}+\frac{1}{r}R_r+\left(m^2-\frac{1}{r^2}\right)R=0\,,\quad \left(\frac{1}{N(z)^2-\omega^2}Z_z\right)_z+\frac{m^2}{\omega^2-f^2}Z=0\,, \qquad (2.18)$$

where the subscripts denote derivatives and

$Z_z = 0$, on z = 0, $-D_e$ for the deep water, and (2.19)

$Z_z = 0$, on z = 0, $-(D_e - h_m)$ for the shallow water over the seamount.

These conditions on Z determine the eigenvalues m_{sj} on the shallow side, and m_{dj} on the deep side, where $j = 1,2,3,\ldots$ $m = 0$ is also an eigenvalue, and corresponds to the barotropic mode. For a given value of m, the solutions for $R(r)$ are Bessel functions, except for $m = 0$, when they are $R(r) = r$ and $1/r$.

Hence, if we assume that the dynamics are inviscid and the internal wave motion over the seamount consists of standing waves (i.e. "sloshing modes"), we may express the solution in the form

$$p_p(r,z) = C_0 \frac{r}{a} + \sum_{j=1}^{\infty} C_j J_1(m_{sj} r) Z_{sj}(z), \qquad 0 < r < a, \qquad (2.20)$$

$$= D_0 \frac{a}{r} + \sum_{j=1}^{\infty} D_j H_1^{(1)}(m_{dj} r) Z_{dj}(z), \qquad r > a,$$

and similarly for $p_m(r,z)$ but with S_j , E_j replacing C_j , D_j respectively, for $j = 0, 1, 2,\ldots$ Here J_1 denotes the familiar Bessel function, and $H_1^{(1)}$ the Hankel function of the first kind. The latter function guarantees that each internal wave mode in the deep water propagates energy away from the seamount to infinity.

The above formulation of the problem is labeled as Case *J*. If we instead take the alternative formulation where the waves over the seamount are assumed to propagate inward and dissipate, the corresponding equations are:

$$p_p(r,z) = \hat{C}_0 \frac{r}{a} + \sum_{j=1}^{\infty} \hat{C}_j H_1^{(2)}(m_{sj} r) Z_{sj}(z), \qquad 0 < r < a, \qquad (2.21)$$

$$= \hat{D}_0 \frac{a}{r} + \sum_{j=1}^{\infty} \hat{D}_j H_1^{(1)}(m_{dj} r) Z_{dj}(z), \qquad r > a,$$

and similarly for $p_m(r,z)$, with $\hat{S}_j, \hat{E}_j$ replacing $\hat{C}_j, \hat{D}_j$ respectively, for $j = 0, 1, 2, \ldots$ This second case is known as Case $H(2)$ (where these labels refer to the Bessel functions involved over the summit). Note that $H_1^{(2)}$ becomes singular at the origin $r = 0$, and hence does not give a realistic description of the baroclinic motion over the seamount. However, this baroclinic motion is found to be small and relatively inconsequential, so that this consideration is not significant. This $H(2)$ model is preferred for the calculation of the baroclinic tide in the deep water.

In order to complete the solutions, it remains to determine the constants C_j, D_j etc. from the boundary conditions at $r = a$. It is readily shown that, for arbitrary $N(z)$, $Z_{dj}(z)$ and $Z_{sj}(z)$ have the following properties (see for example Llewellyn Smith and Young 2002):

$$\int_{-D_e}^{0} Z_{dj}(z)\mathrm{d}z = 0 \ , \qquad i = 1, 2, 3, \ldots$$

$$\int_{-D_e}^{0} Z_{di}(z) Z_{dj}(z) dz = 0, \quad \text{if } i \neq j\ , \qquad (2.22)$$

$$m_{dj}^2 \int_{-D_e}^{0} Z_{dj}^2 \mathrm{d}z = \left(\omega^2 - f^2\right) \int_{-D_e}^{0} \frac{1}{N(z)^2 - \omega^2} \left(\frac{\mathrm{d}Z_{dj}}{\mathrm{d}z} \right)^2 \mathrm{d}z\,,$$

with the same applying to Z_{sj} but with $D_e - h_m$ replacing D_e in the above. Continuity of p_p across $r = a$ above the seamount then gives, for Case J,

$$C_0+\sum_{j=1}^{\infty}C_jJ_1(m_{sj}a)Z_{sj}(z)=D_0+\sum_{j=1}^{\infty}D_jH_1^{(1)}(m_{dj}a)Z_{dj}(z),\quad -(D_e-h_m)<z<0. \qquad (2.23)$$

Integrating this equation over the range $-(D_e - h_m) < z < 0$ gives

$$C_0=D_0+\frac{1}{D_e-h_m}\sum_{j=1}^{\infty}\gamma_{0j}D_j\ . \qquad (2.24)$$

Multiplying (2.23) by $Z_{sk}(z)$ and integrating over the same range gives

$$C_k=\frac{1}{\beta_k}\sum_{j=1}^{\infty}\gamma_{kj}D_j\ ,\qquad k=1,2,3,\ldots \qquad (2.25)$$

where

$$\beta_k=J_1(m_{sk}a)\int_{-(D_e-h_m)}^{0}Z_{sk}^2\mathrm{d}z\,,\ \gamma_{0j}=H_1^{(1)}(m_{dj}a)\int_{-(D_e-h_m)}^{0}Z_{dj}\mathrm{d}z\,,\ \gamma_{kj}=H_1^{(1)}(m_{dj}a)\int_{-(D_e-h_m)}^{0}Z_{sk}Z_{dj}\mathrm{d}z\,. \qquad (2.26)$$

The normal velocity condition (2.15, 2.16) gives

$$-D_0\left(1+\frac{f}{\omega}\right)+\sum_{j=1}^{\infty}\left[m_{dj}aH_1^{(1)\prime}(m_{dj}a)-\frac{f}{\omega}H_1^{(1)}(m_{dj}a)\right]D_jZ_{dj}(z)$$

$$=-\frac{i}{2}\left(1-\frac{f^2}{\omega^2}\right),\qquad -D_e<z<-(D_e-h_m)\,, \qquad (2.27)$$

$$=C_0\left(1-\frac{f}{\omega}\right)+\sum_{j=1}^{\infty}\left[m_{sj}aJ_1'(m_{sj}a)-\frac{f}{\omega}J_1(m_{sj}a)\right]C_jZ_{sj}(z),\quad -(D_e-h_m)<z<0,$$

where primes denote derivatives of Bessel functions. Multiplying this equation by $Z_{dk}(z)$ and integrating from $-D_e$ to 0 gives, for the barotropic motion with $k = 0$, $Z_{d0} = 1$,

$$D_0=\frac{i}{2}\frac{h_m}{D_e}\left(1-\frac{f}{\omega}\right)-\frac{1-\dfrac{f}{\omega}}{1+\dfrac{f}{\omega}}\left(1-\frac{h_m}{D_e}\right)C_0\,, \qquad (2.28)$$

and for $k = 1, 2, 3, \ldots$,

$$D_k\left[m_{dk}aH_1^{(1)\prime}\left(m_{dk}a\right)-\frac{f}{\omega}H_1^{(1)}\left(m_{dk}a\right)\right]\int_{-D_e}^{0} Z_{dk}^2\mathrm{d}z=-\frac{i}{2}\left(1-\frac{f^2}{\omega^2}\right)\int_{-D_e}^{-(D_e-h_m)} Z_{dk}\mathrm{d}z$$

$$+C_0\left(1-\frac{f}{\omega}\right)\int_{-(D_e-h_m)}^{0} Z_{dk}\mathrm{d}z+\sum_{j=1}^{\infty}\left[m_{sj}aJ_1'\left(m_{sj}a\right)-\frac{f}{\omega}J_1\left(m_{sj}a\right)\right]C_j\int_{-(D_e-h_m)}^{0} Z_{sj}Z_{dk}\mathrm{d}z\,. \quad (2.29)$$

Substituting C_0 and C_j from (2.24, 2.25) in these equations gives

$$\sum_{k=1}^{M_d}\left[\delta_{jk}A_{dj}-g_{d0j}\gamma_{0k}-\sum_{i=1}^{M_s}g_{dij}\gamma_{ik}\right]D_k=Q_{dj}, \qquad j = 1, 2, \ldots, M_d, \quad (2.30)$$

where δ_{jk} is the Kroneker delta: $\delta_{jk} = 1$ if $j = k$, $\delta_{jk} = 0$ otherwise, and

$$A_{dj}=\left[m_{dj}aH_1^{(1)\prime}\left(m_{dj}a\right)-\frac{f}{\omega}H_1^{(1)}\left(m_{dj}a\right)\right]\int_{-D_e}^{0} Z_{dj}^2\mathrm{d}z\,, \qquad (2.31)$$

$$Q_{dj}=\frac{i\left(1-\dfrac{f^2}{\omega^2}\right)}{2-\dfrac{h_m}{D_e}\left(1-\dfrac{f}{\omega}\right)}\int_{-(D_e-h_m)}^{0} Z_{dj}\mathrm{d}z\,, \quad g_{d0j}=\frac{1-\dfrac{f^2}{\omega^2}}{2-\dfrac{h_m}{D_e}\left(1-\dfrac{f}{\omega}\right)}\frac{1}{D_e-h_m}\int_{-(D_e-h_m)}^{0} Z_{dj}\mathrm{d}z\,, \quad (2.32)$$

$$g_{dij}=\frac{1}{\beta_i}\left[m_{si}aJ_1\left(m_{si}a\right)-\frac{f}{\omega}J_1\left(m_{si}a\right)\right]\int_{-(D_e-h_m)}^{0} Z_{si}Z_{dj}\mathrm{d}z\,. \qquad (2.33)$$

Here, instead of being taken from 1 to infinity, from the viewpoint of summing these series numerically the sums are taken from 1 to M_d or M_s, depending on whether the sum is over modes in the deep water, or in the shallow water over the seamount. From both practice and common sense, M_d and M_s need to reflect the same resolution, or same spatial scale, so that, in general,

$$M_s \approx M_d(1-h_m/D_e). \qquad (2.34)$$

Equation (2.30) is then solved for the D_j at the required resolution, and then D_0, C_0 are obtained from (2.24, 2.28), and C_j from (2.25). For most purposes in this paper, M_d is taken as 150, and then M_s from (2.34).

The above equations only describe the method of solution for the function p_p for Case *J*. To obtain p_m for Case *J,* one takes the same equations but with $(-f)$ replacing f, obtaining S_j, E_j in place of C_j, D_j. For Case *H*(2), one obtains $\hat{C}_j, \hat{D}_j$ for p_p from the same procedure as above, but with $J_1(m_{sj}a)$ replaced by $H_1^{(2)}(m_{sj}a)$. For p_m for Case *H*(2), one obtains $\hat{S}_j, \hat{E}_j$ from the same equations as for p_p but with f replaced by $(-f)$.

The energy flux radiating away from the seamount for case *J* is given by

$$Eflux = \int_0^{2\pi}\int_{-D_e}^{0}\left[\mathrm{Re}(p_i)\mathrm{Re}(u_r)\right]r\mathrm{d}z\mathrm{d}\theta \ , \tag{2.35}$$

where the integral is taken at some arbitrary radius $r > a$, and

$$Eflux = \rho_0 \omega a^2 U^2 D_e \frac{2}{\left(1-\dfrac{f^2}{\omega^2}\right)} \frac{1}{D_e} \sum_{j=1}^{\infty} \int_{-D_e}^{0} Z_{dj}^2 \mathrm{d}z \frac{1}{2\pi}\int_0^{2\pi} Term.d\theta \quad , \tag{2.36}$$

where

$$Term = D_j D_j^* + E_j E_j^* + (D_j E_j^* + D_j^* E_j)\cos 2\theta + i.(D_j E_j^* - D_j^* E_j)\sin 2\theta \, , \tag{2.37}$$

and the asterisks denote the complex conjugate. This *Term* gives the angular dependence of the energy flux, and the $\sin 2\theta$ and $\cos 2\theta$ terms sum to zero when integrated over all azimuths. In general, the direction of maximum flux is aligned with that of the barotropic tide ($\theta = 0$), with minima at $\theta = \pm \pi/2$, for all modes. However, as $f/\omega \rightarrow 1$ where the flow is close to the inertial resonance, for the lowest order modes this direction moves to positive angles, and for mode 1 it may reach values in excess of 1 radian close to the limit. For the corresponding expression for case $H(2)$, one obtains (2.35-7) but with $\hat{D}_j, \hat{E}_j$ in place of D_j, E_j. In this case there is also energy propagating inward from the boundary of the seamount, and the total of this flux is given by

$$Eflux = \rho_0 \omega a^2 U^2 (D_e - h_m) \frac{2}{\left(1 - \frac{f^2}{\omega^2}\right)} \sum_{j=1}^{\infty} \left[\hat{C}_j \hat{C}_j^* + \hat{S}_j \hat{S}_j^*\right] \frac{1}{(D_e - h_m)} \int_{-(D_e - h_m)}^{0} Z_{sj}^2 \mathrm{d}z \text{ , (2.38) .}$$

This flux is relatively small, as discussed below.

3. Results for Individual Seamounts.

Flow field properties

As shown above, the barotropic tidal pressure field that coexists with unidirectional background barotropic flow (2.1) may be written

$$p_b = \rho_0 U \omega a \frac{r}{a} \frac{i}{2} \left[\left(1 + \frac{f}{\omega}\right) \mathrm{e}^{i\theta} + \left(1 - \frac{f}{\omega}\right) \mathrm{e}^{-i\theta} \right] \mathrm{e}^{-i\omega t} \text{ ,} \qquad (2.13)$$

which consists of a *cum sole* component ($\mathrm{e}^{-\mathrm{i}(\theta + \omega t)}$ in the northern hemisphere) of magnitude proportional to $(1 - |f|/\omega)$, and a *contra sole* component with magnitude proportional to $(1 + |f|/\omega)$. The relative magnitudes are equal at the equator, but the *contra sole* component for the pressure is the larger in each hemisphere, and becomes increasingly dominant with increasing latitude. From (2.20) and (2.21), the barotropic component of $\boldsymbol{u_i}$ over the seamount has a similar form to (2.13), and in the deep water it resembles potential flow around the seamount. The corresponding internal tide p_i may be expressed as

$$p_i = \rho U \omega a[p_m(r,z)\mathrm{e}^{i\theta} + p_m(r,z)\mathrm{e}^{-\mathrm{i}\theta}]\mathrm{e}^{-i\omega t}, \tag{2.14}$$

where the p_p component is forced by the $\mathrm{e}^{i(\theta-\omega t)}$ term in (2.15), and the p_m component by the $\mathrm{e}^{-i(\theta+\omega t)}$ term. Accordingly, we may expect the baroclinic *contra sole* pressure component to dominate over the *cum sole* component except near the equator because the respective forcing terms are larger. However, as shown below this is not normally the case.

Two types of stratification are considered here. First, N is assumed uniform everywhere, to give the simplest description of the flow types and a base for the energy flux results. For this case, the eigenfunctions for the vertical structure are given by

$$Z_{dj}(z) = \cos\left(\frac{j\pi z}{D_e}\right), \quad Z_{sj}(z) = \cos\left(\frac{j\pi z}{D_e - h_m}\right), \quad j = 1, 2, 3, \ldots.. \tag{2.39}$$

Second, stratification with uniform N but with a surface mixed layer and shallow thermocline is discussed. For the uniform N case we may identify four main dimensionless parameters for individual seamounts: f/ω, ω/N, h_m/D_e, and $\omega a/ND_e$, where the last may be identified as a form of Burger number for this system. In general, the quantities ω, N and D_e have reasonably well-defined values for the ocean, but f, h_m and a depend on the location and shape of the seamount. We take $D_e = 4$ km, and $\omega = 1.41.10^{-4}$ rad/sec, focusing on the semi-diurnal tide, with $N = 10^{-3}$ rad/sec for definiteness. Hence

ω/N is chosen, or deemed to have a narrow range of values. We consider seamounts that have a maximum radius of about 100 km, unusually large for a seamount. Hence, for the other parameters the computations need to cover the ranges of values as follows: $0 < f/\omega < 1$, $0 < h_m/D_e < 1$, and $0 < \omega a/ND_e < 5$.

Before describing the results of computations for these ranges of variables, we first examine the nature of the baroclinic tide generated by two representative seamounts where $f/\omega = 0.5$, $\omega a/ND_e = 0.5$, and $h_m/D_e = 0.8$ and 0.2. In all cases with this topography, the flow is dominated by an axisymmetric pattern of conical rays with slope c that originate from the tangent point of these rays with the summit rim, as illustrated schematically in Figure 2 . Although the flow is computed as a sum of modes consisting of Hankel (Bessel) functions radially and cosines vertically, they sum to give this distinct conical pattern (with apex above the seamount) with rapid transitions in flow across the boundaries of the cone. The more modes that are included in this sum, the sharper are the transitions across the boundaries of this cone and its continuations by reflection at the top and bottom boundaries of the fluid. These conical regions contiguous with the region over the seamount tend to contain larger velocities, and show phase propagation in the velocity that is consistent with energy flux away from the seamount, at all azimuthal positions. This is consistent with two-dimensional solutions for steep topography. The solution is calculated in terms of two distinct functions of r and z: one contra-sole (u_p, p_p if f positive), the other cum sole (u_m, p_m). Here the velocities u_p and u_m have similar magnitudes (though they are not identical), but the cum-sole pressure p_p has larger amplitude than the contra-sole. This difference increases with increasing h_m/D_e.. This is the opposite situation for the pressure function for the barotropic tide in equation (2.13), and occurs because the cum-sole component is closer to the inertial resonance at $\omega = f$.

Figure 3 shows a sample of the flow for the case with $h_m/D_e = 0.8$, for a vertical section along the seamount axis aligned with the barotropic tidal flow direction on the downstream side ($\theta = 0$), with Figure 3a showing the amplitude of the total velocity and Figure 3b the phase. The flow has obvious similarities to the two-dimensional case, with upward phase propagation in the downward-sloping beam, and smaller velocities in the broad region below it. Figure 4 shows the amplitude (figure 4a) and the phase (figure 4b) of the radial velocity for the same flow but at azimuthal longitude $\theta = 90^{\circ}$. Here the velocities are much weaker, but the rays emanating from the summit rim are quite conspicuous, and show virtual discontinuities in phase and amplitude across them. Upward phase propagation, implying downward energy propagation from linear wave theory, is again apparent in the beam emanating from the region above the summit. In contrast, Figures 5 and 6 show the corresponding flow patterns for the same parameters but with $h_m/D_e = 0.2$. Here the narrow "beam" containing most of the structure emanates from the topography, rather than the region above the summit. Inside it the amplitude of the radial velocity is low, and its phase propagation is opposite to that expected from linear wave theory. In the broader regions between, the radial velocity is much larger, and has outward phase propagation as expected. The constituent modes of these flows each have outward energy propagation, but when these are summed to give the overall spatial pattern, the phase propagation in the various regions delineated by the rays from the upper seamount edge may differ from what one might expect, and also vary with the variable (*p*, *u,* or *v*) considered. The amplitude of the baroclinic motion is small in the "shadow region" adjacent to the steep sides of the topography, in each of the figures of Figure 4. If most of these regions beneath the downward-sloping rays from the summit rim were filled in with solid topography, little change would be expected in the remaining solution elsewhere. This provides good justification for the steep-sided pillbox model for seamounts.

Energy Fluxes

We consider primarily the H(2) case (with inward-propagating energy flux over the summit), focusing on the baroclinic energy flux away from the seamount, and present the energy flux in terms of the dimensionless variables h_m/D_e, $a\omega/ND_e$ and f/ω as calculated from equation (2.36). Although the results for the energy flux were computed in terms of $\rho_0\omega a^2U^2D_e$, it turns out to be more appropriate to present them in terms of $\rho_0NaU^2D_e^2$. Fluxes in the limit of large $a\omega/ND_e$ are shown in Figure 7. These results were computed for $a\omega/ND_e = 20$, but are a good approximation for $a\omega/ND_e > 1$, as comparison with Figure 8 and 9 shows. The curve for small f/ω is approximately described by the function $[\sin(\pi(1-h_m/D_e))/(2-h_m/D_e)]^2$, which is contained in the equations of section 2, but there does not seem to be an obvious analytic extension that includes f/ω. As f/ω increases above about 0.4, the maximum of the curves moves to larger values of h_m/D_e, shrinking to small values as f/ω approaches unity. This energy flux must necessarily be zero when either f/ω or $h_m/D_e = 1$.

The three-dimensional structure of this energy flux with the same scaling is shown for $a\omega/ND_e < 1$ in Figures 8 and 9 as a function of the seamount shape parameters h_m/D_e, $a\omega/ND_e$. These curves level off in the direction of increasing $a\omega/ND_e$, so that the dimensional energy flux increases linearly with a for $a\omega/ND_e > 0.5$, approximately. For small $a\omega/ND_e$, these curves increase quadratically with $a\omega/ND_e$, so that the energy flux increases with a^3 for $a\omega/ND_e \ll 1$, up to about 0.3. As a function of f/ω, these curves have their largest amplitude near $f/\omega = 1$, as shown in Figure 9 (where all curves have the same scale), though they descend rapidly to zero as this limit is approached. This is clearly associated with inertial resonance, and is discussed further below. Some computations in which N and D_e were each varied by an order of magnitude gave essentially the same dimensionless magnitudes as given in these figures, so that this scaling is robust for these variables, as expected.

The above results have been compared with those from the *J*-model, in which the motion over the seamount is composed of stationary oscillations for all modes. The energy flux results are very similar, with magnitudes differing by a few percent. There are, however, small systematic differences which are shown in Figure 10, a representative example with $f/\omega = 0.3$; as in Figure 8 for the $H(2)$ model, corresponding figures for f/ω ranging from 0 to 0.5 are similar to this one. Figure 10 may be compared with Figure 8b. The radiated energy flux plot in the *J*-model contains small ridges and valleys that are approximately straight on this diagram. These linear ridges approximately correspond with the zeroes of the Bessel function $J_1(m_{si}a)$, the first zero with the first ridge, the second zero with the second, and so on. Hence these ridges correspond with near-resonances associated with the forcing of the stationary modes over the seamount, the structure of which has the form of this Bessel function. In the inviscid theory these are not full resonances, as the energy is always able to leak away across the open boundary at the edge of the seamount, but as the computations show, a small maximum in the energy flux results.

Figure 11 shows a representative distribution of the total energy flux across the internal wave modes. Here $h_{m,}/D_e = 0.8$, $f/\omega = 0.5$, $a\omega/ND_e = 1$, model $H(2)$ is used, and 150 modes are taken. This "energy spectrum" has similar character to those for a two-dimensional knife-edge ridge (St. Laurent et al., 2003). For this tall seamount, much of the energy is in mode 1, with a power law decrease with increasing mode number. As for the 2D ridge there is also an oscillation in this amplitude, with a period of several modes (ten in this case) that remains approximately constant as the mode number increases.

The nature of the flow over the seamount

For the $H(2)$ model, where inward propagation from the seamount edge is assumed, the baroclinic motion over the seamount is not realistic, but it is not large. The inward energy fluxes from (2.36) are much smaller than the external ones. As figures 3-6 indicate, the baroclinic motion over the summit is small compared with the barotropic – there is little structure evident inside the conical beams radiating from the shallow region above the summit. Hence the main feature of interest is the structure of the barotropic motion over the seamount, forced by the external barotropic tide, and determined by the complex coefficients C_0 and S_0 in the expressions for p_p and p_m of equation (2.20). Three factors of practical interest are considered here: the magnitude of this barotropic perturbation, the orientation of the largest motion, and its phase relative to the original barotropic forcing.

Here it is appropriate to use Cartesian coordinates (x,y), with corresponding velocities (u,v). The perturbation barotropic velocity is spatially uniform over the flat top of the seamount, and may be expressed as

$$\frac{u_i}{U} = -\frac{i}{\left(1-f^2/\omega^2\right)}\left[C_0\left(1-\frac{f}{\omega}\right)+S_0\left(1+\frac{f}{\omega}\right)\right]\mathrm{e}^{-i\omega t}, \qquad (3.1)$$

$$\frac{v_i}{U} = \frac{1}{\left(1-f^2/\omega^2\right)}\left[C_0\left(1-\frac{f}{\omega}\right)-S_0\left(1+\frac{f}{\omega}\right)\right]\mathrm{e}^{-i\omega t},$$

for the velocity components in the x and y directions, with magnitudes

$$\left|\frac{C_0}{1+f/\omega}+\frac{S_0}{1-f/\omega}\right|, \quad \left|\frac{C_0}{1+f/\omega}-\frac{S_0}{1-f/\omega}\right|, \qquad (3.2)$$

respectively. We first note the magnitude of this quantity for the case where there is no stratification (*i.e.* $N = 0$). Here (2.24, 2.28) give $D_0 = C_0$, $E_0 = S_0$, and

$$C_0 = \frac{\frac{i}{2}\frac{h_m}{D_e}\left(1-\frac{f^2}{\omega^2}\right)}{2-\frac{h_m}{D_e}\left(1-\frac{f}{\omega}\right)}, \quad S_0 = \frac{\frac{i}{2}\frac{h_m}{D_e}\left(1-\frac{f^2}{\omega^2}\right)}{2-\frac{h_m}{D_e}\left(1+\frac{f}{\omega}\right)} \,. \qquad (3.3)$$

Adding the initial barotropic velocity, the total velocity over the seamount for this unstratified case is, for this model,

$$u = U\cos\omega t\left[1+\frac{h_m}{D_e}\frac{2-\left(\frac{h_m}{D_e}\right)^2\left(1-\frac{f^2}{\omega^2}\right)}{4\left(1-\frac{h_m}{D_e}\right)+\left(\frac{h_m}{D_e}\right)^2\left(1-\frac{f^2}{\omega^2}\right)}\right],$$

$$v = -U \sin \omega t \frac{h_m}{D_e} \frac{f}{\omega} \frac{2}{4\left(1-\frac{h_m}{D_e}\right)+\left(\frac{h_m}{D_e}\right)^2\left(1-\frac{f^2}{\omega^2}\right)}. \qquad (3.4)$$

These expressions are independent of the seamount radius a, and give *cum-sole* elliptical motion over the seamount, with the major axis aligned with the external barotropic flow. This barotropic flow, with potential flow in the deep water, is illustrated in Figure 12 for the parameter values $h_m/D_e = 0.8, f/\omega=0.5$. For tall seamounts where h_m/D_e approaches unity so that the depth of the seamount top is a small fraction of the total depth, this is approximated by

$$u \approx U \cos \omega t \left[1+\frac{1+f^2/\omega^2}{1-f^2/\omega^2}\right], \quad v \approx -U \sin \omega t \left[\frac{2f/\omega}{1-f^2/\omega^2}\right]. \qquad (3.5)$$

The perturbation increases dramatically as the cut-off latitude (where $\omega = f$) is approached, due to tidal forcing at the inertial resonance. This implies that, even when there is no stratification, the diurnal tide should be large over seamounts near the cut-off latitude of 30°. Large amplification of the diurnal tide (up to a factor of 10) has been observed over the Great Meteor Seamount (summit width 31 km), centred at latitude 30°S in the South Atlantic (Mohn and Beckmann, 2002), and over the smaller Fieberling Guyot (summit width 10km, latitude 32° 27'N) in the North Pacific (Brink 1995).

For seamounts of small radius, the presence of stratification and the forcing of the internal modes radiating energy away from the seamount can cause changes to the barotropic motion over it. The magnitude of the x-component perturbation u_i/U is shown in Figure 13 for a range of values of f/ω: 0, 0.3, 0.6 and 0.95. For most of the parameter range, (3.4) gives a good description of this variable, the exceptions being when the seamount radius is small and, approximately,

$$h_m/D_e > 2a\omega/ND_e. \qquad (3.6)$$

In this range, the velocity is smaller than the homogeneous value given by (3.4). Computations of the phase of this maximum (not shown) show that it is significantly negative, particularly for small $a\omega/ND_e$ where it reaches values near $-\pi/2,$ implying that it occurs ¼-cycle earlier. The amplitude of the v-velocities are shown in Figure 14, for the values f/ω = 03, 0,6 and 0.95 (the value for f/ω =0 being zero). As for the u-velocities, the values for v are well-described by (3.4), except when (3.6) applies, when they are generally smaller as seen in Figure 14. The phases are approximately $\pi/2$ from those for $u_{\text{i.}}$ Hence, the velocities over the seamount are generally well-described (apart from phase) by (3.4), except when h_m/D_e is large and $a\omega/ND_e$ is small.

If the above quantities are computed with the J-model, incorporating standing baroclinic oscillations over the seamount, the curves obtained are very similar to those of Figures 13 and 14, with some small oscillations superimposed, much like the comparison of Figure 10 with Figure 8. Hence these results for this barotropic flow may be regarded as robust. For the J-model it is possible to calculate the baroclinic modes, and (for the pressure variable) these are smaller than the barotropic. The largest is usually the first baroclinic mode with coefficient S_1, which may become noticeable for small values of $a\omega/ND_e$, implying that the gravest baroclinic mode may be significant for small seamounts, but not others. For wide seamounts (large a), the presence of dissipation will degrade the possibility for coherent modes in any case.

Variable stratification

Some computations were carried out with a density profile that incorporated a surface mixed layer, and a shallow thermocline modelled as an interface at the bottom of the mixed layer. Here the relevant parameters are $d/(D_e - h_m)$, where d is the mixed layer thickness, and $G = g'/\omega^2 D_e$, where $g' = g\Delta\rho/\rho_0$ and $\Delta\rho$ is the density difference across the interface. These were done with a seamount with a summit 500 m below the surface; the depth of the interface was varied from zero to a level just above the seamount top, and the interface strength G was varied from 0 to 20. For these variables, a surface mixed layer that is created by mechanical stirring without surface buoyancy flux satisfies $d/D_e = (\omega/N)^2 G$, which lies within these ranges of values.

The results were initially surprising. Although these variations caused expected changes in the form of the internal tide field from the changes in the density structure and the associated modes, the total energy flux varied by only a few percent. This insensitivity of the radiated energy flux to the stratification above the seamount is consistent with the above result that the main forcing for the internal tides is associated with the barotropic motion there.

4. Seamount distributions and integrated results.

A global distribution of seamounts as inferred from satellite altimetry has been given by Wessel (2001). Various studies of seamount morphology have concluded that a typical seamount is closely approximated by a flat-topped cone with a flank slope of 17°, and a ratio of height h_m to radius a of the flat top of

$$h_m/a = 0.69, \qquad (4.1)$$

which may be termed the "Wessel relation". Wessel identifies nearly 15,000 seamounts by satellite altimetry, and they have a distribution in height as shown in Figure 15. They are also consistent with a power law proposed by Wessel and Lyons (1997) of the form

$$N_{pl} = 6.10^4 / h_m^{4.16}, \qquad (4.2)$$

where N_{pl} denotes the number of seamounts in 250 m bands in height. This relationship is also shown in Figure 15, and fits the data for $h_m > 2$ km. Its extrapolation to the range $h_m = 1$-2 km, where existing satellite altimetry resolution is inadequate for detecting seamounts, suggests that the total number is closer to 100,000, mostly made up by seamounts with heights smaller than 2 km.

Since (4.1) approximates many seamounts in the ocean, it is appropriate to examine the properties of the internal tides generated by these seamounts in more detail. They are too small to conform to the wide seamount limit ($a\omega/ND_e > 1$), and are represented by a section across the diagrams of Figures 8-10. Figure 16 shows the total energy flux for these seamounts as functions of h_m/D_e and f/ω; the character is similar to the wide-seamount limit of Figure 7. With realistic values of the parameters, these results show that individual seamounts generate fluxes of order 10^6 Watt for linearly polarized tidal currents of 1 cm/sec. As Figure 11 indicates, most of the energy flux radiated from a seamount is contained in a small number of the lowest modes. Results are presented here for the three lowest modes. Figure 17a shows the total energy flux radiated by the first mode (vertical structure given by (2.39)), and this is clearly a substantial fraction of the total for most values of the parameters. This radiation is not uniform with azimuthal position around the seamount, and has cos $2(\theta-\alpha_1)$ dependence on θ. The angle α_1 of maximum energy flux is shown in Figure 17b, and the maximum and minimum values of this elliptical distribution are plotted in Figure 17c. Corresponding results for modes 2 and 3 are shown in Figures 18 and 19 respectively. The shape of the mode 1 energy flux curves in Figure 17a are generally similar to those for the total energy flux shown in Figure 16. For most situations, the direction α_1 of the maximum of this flux is slightly positive (i.e rotated anti-clockwise) relative to the x-axis by up to 15 degrees. If $f/\omega = 0$, this energy flux is bi-directional along the *x*-axis, but as f/ω increases the ellipticity of the distribution decreases and it becomes more azimuthally uniform, as shown in Figure 17c. For modes 2 and 3, some of the energy flux curves show a second maximum near $h_m/D_e = 0.5$; the values of α_2 and α_3 are also somewhat larger, and may be negative (*i.e.* clockwise relative to the barotropic tide direction) for f/ω near unity. These curves for the three modes give a good indication of the nature and location of most of the internal wave field and associated energy flux around these seamounts.

In order to estimate the total baroclinic energy flux generated by the sum of these seamounts, we consider the height ranges given by Wessel, and employ the model of the previous sections. For a linearly polarized barotropic tidal flow with velocity of magnitude U, the energy flux radiated from the seamount is given by

$$Eflux = F\left(\frac{h_m}{D_e}, \frac{a\omega}{ND_e}, \frac{f}{\omega}\right)\rho_0 aN(UD_e)^2, \qquad (4.3)$$

where the function F is plotted in Figure 16 for $D_e = 4$ km. Here we take $U = 1$ cm/sec, and $D_e = 4.5$ km. Most seamounts lie in latitudes of less than 60°, and as Figure 16 shows, the dependence of the energy flux on f is not large unless f/ω is close to unity, so we assume that $f/\omega = 0.5$ for all seamounts for these computations, giving the F curve shown in Figure 20a. Equation (4.3) then gives energy fluxes for individual seamounts, as also shown in Figure 20a. Multiplying these fluxes by the number of seamounts in the 250 m height ranges shown in Figure 15, according to the two seamount number-models, gives the total sum of the energy flux in each range box, which is shown in Figure 20b. Summing over all of the boxes then gives the total energy flux, for each number-model. The results are $1.8.10^9$ Watt for the satellite altimeter seamount count, and $2.4.10^9$ Watt for the power law model.

If the tide were circularly polarized with the same strength, the fluxes would be double these values. Also, this velocity is at the lower end of ranges of mid-ocean barotropic tidal velocities, and the flux will be larger in regions with larger U. The result is not as sensitive to the chosen value of D_e as equation (4.3) suggests. A seamount situated on a mid-ocean ridge where the effective depth is less than over an abyssal plane will have a correspondingly larger value of U, which will compensate for the depth decrease – the barotropic tidal volume flux UD_e will remain effectively constant, and only vary with the large-scale pattern of the barotropic tide. Accordingly, the above expression is seen to be reasonably robust.

These numbers may be compared with the estimates of internal tide generation from continental slopes, and from the Hawaiian ridge. Internal tidal energy flux from continental slopes has been estimated as 1.45×10^{10} Watt for the M_2 tide, and 2.73×10^9 Watt for the S_2 tide (Baines 1982). For the whole Hawaiian ridge, the corresponding flux for the M_2 tide is estimated to be 2x10^{10} Watt (Rudnick et al. 2003), a very similar number to that from the sum of continental slopes. For the nett total from all the seamounts, we cannot make a direct comparison without a more careful estimate of the magnitudes of the background barotropic tide in the locations of the seamounts, but if we assume a circularly polarized barotropic M_2 tide, the above numbers (from this section) give 5x10^9 Watt, which is less than those of the continental shelves and Hawaiian ridge, but is comparable with them.

5. Comparison with previous models.

The energy flux results of section 4 are presented in the most appropriate form for seamounts, but this differs from that which arises naturally from linear perturbation theory. In particular, Llewellyn-Smith and Young (2002) derive the energy fluxes from linearised seamounts of Gaussian shape

$$h = h_m e^{-(x^2+y^2)/2a^2} \quad , \tag{5.1}$$

and for the same external conditions as used above for the pillbox model, obtain

$$Eflux = G\rho_0 N a U^2 h_m^2 \left(1-\left(\frac{f}{\omega}\right)^2\right)^{1/2} , \tag{5.2}$$

where a is now the Gaussian width of an axisymmetric seamount, and G is a function of a parameter A defined as

$$A = \pi \frac{a\omega}{ND_e}\left(1-\left(\frac{f}{\omega}\right)^2\right)^{1/2} . \tag{5.3}$$

For present purposes, G is given approximately by

$G = 0.696, \qquad 0 < A < 1,$

$$\approx \frac{\pi}{2} A^3 \left(e^{-A^2} + 4e^{-4A^2} \right), \quad A > 1. \tag{5.4}$$

G decreases rapidly from 0.696 as A increases beyond unity, and is effectively zero for $A>3$.

The corresponding results from two-dimensional ridges are often presented in the same manner. In particular, for a 2-D knife-edge ridge, for a length of ridge $2a$ (to be compared with seamounts of this diameter) the energy flux is given by (5.2) but with G replaced by a function G_{kn}, which only depends on h_m/D_e and increases monotonically from $\pi/2$ (St. Laurent et al. (2003), Llewellyn-Smith and Young (2003)). G_{kn} is shown plotted in Figures 21a and b.

Figure 21a shows the results for the pillbox model, presented in the same manner, for a range of values of f/ω and for $a\omega/ND_e > 1$ (wide seamounts). The function G_{kn} and the maximum value of G are shown dashed, for comparison. It is clear that this form of scaling is not particularly appropriate for seamounts, as these curves vary substantially with h_m/D_e, though they do tend to coalesce for f/ω small. There is a weak singularity at the origin with the approximate form $1/h_m^{0.1}$. Compared with the knife-edge ridge, these curves decrease with increasing height because the fluid can pass around the seamount rather than over it. Interestingly, the pillbox values are generally larger than the Gaussian linear ones for small f/ω, and this may also be the case for larger f/ω for wide seamounts, depending on equation (5.4).

Figure 21b shows the corresponding curves for Wessel's observed ratio $h_m/a = 0.69$ (i.e.

the parameter $a\omega / ND_e = (\omega / 0.69N)h_m / D_e$ (for these parameter values, the plotted value of G is the valid one). In these cases both the 2-D and linearised models give substantially larger energy fluxes than the pillbox model, for all seamount heights except for large, high seamounts when the system is close to the inertial resonance. This is, again, a reflection of the fact that steep-sided seamounts tend to deflect the barotropic tide around them, an effect not fully captured by linearised topography.

6. Summary and discussion.

I have described a model of internal tidal generation over steep-sided axisymmetric topography that is applicable to seamounts. In this model the seamounts are pillbox-shaped, with flat top and vertical sides. Two versions of the model have been compared: one in which the generated internal waves over the seamount form standing modes, and one in which they are assumed to propagate inwards from the summit rim and decay. The latter is preferred for most purposes here, but the two models give similar answers for the structure and amplitude of the waves radiating away from the seamount, and the associated energy flux. The reason for this is due, at least in part, to the fact that the waves radiating away in the deep water are primarily forced by the forced barotropic motion over the seamount. For this simple topography, this barotropic motion is spatially uniform over the seamount. For $h_m/D_e < 2a\omega/ND_e$, it is independent of the stratification, and is given by the simple expressions for zero stratification (3.4). However, this relationship is not satisfied for most seamounts in the ocean, where the radiated energy loss due to the stratification causes a reduction in the barotropic motion over the seamount. This occurs because the radiated energy loss from a seamount tends to reduce the amplitude of the barotropic motion over the seamount that (primarily) forces it, and this effect becomes more significant as the radius of the seamount becomes smaller. This motion over the seamount becomes large for diurnal tides near 30° latitude, and this is consistent with observations.

The pattern of internal waves produced by the linearly polarized barotropic tidal flow past a seamount consists of an axisymmetric conical beam radiating along "characteristics" or wave rays from the region over the seamount. A vertical section through this cone shows that the flow (examples of which are shown in Figures 3-6) resembles the familiar pattern from two-dimensional steep topography. There is variation in amplitude and phase with azimuthal angle, the flow having larger magnitude in the x-direction, aligned with the initial barotropic flow, than in the transverse y-direction. In the x-direction in particular, if $h_m/D_e > 0.5$, the amplitude of u in the beam emanating from above the seamount is approximately uniform across the beam, with phase variation of less than 0.3 radians. This is consistent with the beam being primarily generated by the forced barotropic motion over the seamount.

Most seamounts in the ocean conform to the relationship $h_m/a \sim 0.69$, which generally implies that the Burger-number parameter $a\omega/ND_e < 0.2$. For these cases, energy fluxes from individual seamounts are of order 10^6 Watt. Integrating over all of these seamounts gives a total estimate of $2.4.10^9$ Watt for linearised background barotropic flow of 1 cm/sec. If we assume a circularly polarised M_2 tide of this magnitude, the estimate is doubled, but is less than the estimates for energy flux from the sum of continental slopes and from the Hawaiian ridge for M_2, but is comparable with both. The precise value for the seamounts depends on how they are counted, the magnitude and polarization of local barotropic tidal currents, latitude of seamounts etc., but the total order of magnitude seems robust.

Acknowledgements. This work has benefited from discussions with several colleagues, but I would like to specifically mention conversations with Bill Young, which led to improvements in the formulation of the model. Comments from two anonymous referees were helpful in improving the manuscript. This work has been funded in part by the QUEST Programme of the Natural Environmental Research Council of the UK.

References.

Baines, P.G., 1973 : The generation of internal tides by flat-bump topography. *Deep-Sea Res.*, **20**, 179-205.

Baines, P.G., 1974 : The generation of internal tides over steep continental slopes. *Phil. Trans. Roy. Soc.*, London, **277**, 27-58.

Baines, P.G., 1982 : On internal tide generation models. *Deep-sea Res.* **29**, 307-338.

Baines, P.G. and Miles, J.W. 2000: On topographic coupling of surface and internal tides. *Deep-Sea Res.*, **47**, 2395-2403.

Bell, T. H. 1975 Topographically generated internal waves in the open ocean. *J. Geophys. Res.* 80, 320-327.

Balmforth, N.J., Ierley, G.R. and Young, W.R. 2002 Tidal conversion by subcritical topography. *J. Phys. Oceanog.* **32**, 2900-2914.

Brink, K. 1995 Tidal and lower frequency currents above Fieberling Guyot. *J. Geophys. Res.* **100**(C6), 10,817-10,832.

Egbert and Ray 2000 Significant dissipation of tidal energy in the deep ocean inferred from satellite altimeter data. *Nature* **405***,* 775-778**.**

Garrett.C.J.R. and Kunze, E. 2007 Internal tide generation in the deep ocean. *Ann. Rev. Fluid Mech.*, to appear.

Holloway, P. and Merrifield, M. 1999. Internal tide generation by seamounts, ridges and islands, *J. Geophys. Res.* **104**, 25937-25951.

Llewellyn Smith, S.G. and Young, W.R. 2002 Conversion of the barotropic tide. *J. Phys. Oceanog.* **32**, 1554-1566.

Llewellyn Smith, S.G. and Young, W.R. 2003 Tidal conversion at a very steep ridge. *J. Fluid Mech.* **495**, 175-191.

Mohn, C. and Beckmann, A. 2002. The upper ocean circulation at Great Meteor Seamount, Part I: structure and density of flow fields. *Ocean Dyn.* **52**, 179-193.

Morozov, E.G. 1995. Semidiurnal internal tidal wave field, *Deep-Sea Res. I* **42**, 135-148.

Munk, W. and Wunsch, C. 1998. Abyssal recipes II: energetics of tidal and wind mixing. *Deep-Sea Res.* **45**, 1977-2100.

Munroe, J.R. and Lamb, K.G. 2005 Topographic amplitude dependence of internal wave generation by tidal forcing over idealized three-dimensional topography. *J. Geophys. Res*. **110**:10.1029/2004JC002537.

Prinsenberg, S.J. and Rattray, M. Jr. 1975. Effects of continental slope and variable Brunt-Väisälä frequency on the coastal generation of internal tides. *Deep-Sea Res.***22**, 251-265.

Rattray, M. 1960. On the coastal generation of internal tides, *Tellus,* **12**, 54-62.

Ray, R.D. and Mitchum, G.T. 1997. Surface manifestations of internal tides in the deep ocean: observations from altimetry and island gauges, *Prog. Oceanogr.* **40**, 135-162.

Rudnick, D.L. and eightteen others, 2003. From tides to mixing along the Hawaiian ridge, *Science,* **301**, 355-357.

St. Laurent, L., Stringer, S., Garrett, C. and Perrault-Joncas, D. 2003 The generation of internal tides at abrupt topography. *Deep-Sea Res.* I **50**, 987-1003.

Wessel, P. 2001 Global distribution of seamounts inferred from Geosat/ERS-1 altimetry. *J. Geophys. Res.* **106**, 19431-19441.

Wessel, P. and Lyons, S. 1997 Distribution of large Pacific seamounts from Geosat/ERS-1: Implications for the history of intraplate volcanism. *J. Geophys. Re*s. 102, 22,459-22476.

Figure Captions.

Figure 1. The pillbox model of a seamount, with coordinate system.

Figure 2. The pattern of conical rays for the baroclinic tide for a representative seamount.

Figure 3. (a) Amplitude and (b) phase of the total velocity u/U in the x-direction ($\theta = 0$) for the conditions $h_m/D_e = 0.8$, $f/\omega = 0.5$, $a\omega/ND_e = 0.5$, calculated using the $H(2)$ model with 150 modes. The contour interval is 0.2 for (a), and 0.2 radians for (b). The "fuzzy" nature of some of the contours is a consequence of summing a large number of modes.

Figure 4. The same as Figure 3, but for the velocity in the y – direction ($\theta = \pi/2$). The contour interval is 0.05 for (a), 0.4 radians for (b).

Figure 5. As for Figure 3, but with $h_m/D_e = 0.2$. Contour interval is 0.1 for (a), 0.01 radians for (b).

Figure 6. As for Figure 4, but with $h_m/D_e = 0.2$. Contour interval is 0.01 for (a), 0.4 radians for (b).

Figure 7. Energy flux radiating away from the seamount in units of $\rho_0 NaU^2D_e^2$ in the limit of large $a\omega/ND_e$ as a function of h_m/D_e for various values of f/ω. These values were calculated for $a\omega/ND_e$ =20, but are a good approximation for $a\omega/ND_e > 1$.

Figure 8. Energy flux in units of $\rho_0 NaU^2D_e^2$ as a function of h_m/D_e, $a\omega/ND_e$ for various

values of *f/ω*, calculated with the model H(2): (a) *f/ω* =0, (b) 0.3, (c) 0.6, (d) 0.9. Note the change in scale for (d) compared with (a – c).

Figure 9. Energy flux as for figure 8, but with values close to the inertial cut-off. (a) *f/ω* = 9, (b) 0.95, (c) 0.99. (a) is the same as Figure 8(d) and is repeated here for comparison with (b) and (c). The curves are all plotted on the same scale to display the variation when the tidal frequency is close to the inertial frequency.

Figure 10. Energy flux as for figure 8 but for the J-model with stationary modes over the seamount, for *f/ω* = 0.3. Results for *f/ω* < 0.5 are similar. Compared with figure 8b, the additional small ridges and valleys are due to partial resonances of the internal wave modes over the seamount.

Figure 11. The contribution to the total energy flux from various internal wave modes for a seamount with parameters $h_m/D_e = 0.8$, $f/\omega = 0.5$, $a\omega/ND_e = 1$, computed with the *H*(2) model, shown on a log-log scale. Most of the energy flux is carried by a small number of low order modes, and there is a periodic variation with period ~ 10 modes.

Figure 12. Schematic plan view of the stream field of barotropic motion in the absence of stratification, for the parameter values $h_m/D_e = 0.8$, $f/\omega=0.5$, at four phases of the tide: (a) $t=0$; (b) $t = \pi/2\omega$; (c) $t = \pi/\omega$; (d) $t = 3\pi/2\omega$. The slab-like motion of the fluid over the seamount is shown by the central arrows, with potential flow in the deep water. The amplitude of the external barotropic velocity is shown by the arrows at the top of (a) and (c); for these parameters the relative amplitudes over the seamount are 1.95 in (a) and (c), and 0.31 in (b) and (d). With stratification present, this barotropic field is essentially

unchanged if $h_m/D_e < 2a\omega/ND_e$. Otherwise, the motion over the seamount is reduced in amplitude. The internal tide is generated by the mismatch at the summit rim between the slab-like motion over the seamount and the potential flow around it.

Figure 13. The x-component of the maximum perturbation barotropic velocity u_i/U over the seamount as calculated for the $H(2)$ model as a function of the seamount shape parameters and f/ω = (a) 0, (b) 0.3, (c) 0.6, (d) 0.95.

Figure 14. As for Figure 13 but for the velocity v_i/U in the (transverse) y-direction. The case $f/\omega = 0$ is omitted because the values are all zero.

Figure 15. Numbers of seamounts in 250 m height ranges, inferred from satellite altimetry (Wessel 2001), and the extension of these data to the range h_m = 1-2 km by a power law relationship (Wessel and Lyons 1997).

Figure 16. Energy flux radiating away from the seamount in units of $\rho_0 NaU^2 D_e^2$ for seamounts satisfying the "Wessell relation" $h_m/a = 0.69$ (*c.f.* Figure 7).

Figure 17. Properties of the energy flux in mode 1 for seamounts satisfying the Wessel relation. (a) Total energy flux away from the seamount in mode 1, as in Figure 16. (b) Orientation α_1 of the direction of maximum energy flux in mode 1, measured anti-clockwise from the real axis. $\alpha_1 = 0$ for $f/\omega = 0$. (c) Maximum (solid lines) and minimum (dashed) amplitude of the elliptical azimuthal distribution of energy flux. The energy flux

minimum is zero for $f/\omega = 0$. These curves come closer together as f/ω increases, implying that the azimuthal distribution changes from unidirectional to nearly zonally uniform. Contour 0.1 is plotted for (b), but not for (a) and (c).

Figure 18. As for Figure 17, but for mode 2.

Figure 19. As for Figure 17, but for mode 3.

Figure 20. (a) The function $F(h_m/D_e, a\omega/ND_e, f/\omega)$ (plotted as $10F$) for the relation (4.1) with $f/\omega = 0.5$ and $D_e = 4.5$ km, and Energy flux per seamount (by 10^{-6} on the same scale), with the same units as in Figure 16. (b) Total energy flux obtained by summing results from (a) over all seamounts in each 250 m height band, for the numbers shown in Figure 15.

Figure 21. (a) Energy flux for seamounts of radius a, expressed in terms of the factor $\rho_0 NaU^2 h_m^2 \left(1-\left(\frac{f}{\omega}\right)^2\right)^{1/2}$, which arises from linear perturbation theory. The solid curves are for seamounts with $a\omega/ND_\mathrm{e} > 1$, and $f/\omega = 0, 0.3, 0.5, 0.7, 0.8, 0.9, 0.95, 0.99$ in sequence. Upper dashed curve: two-dimensional knife-edge ridge, length $2a$ (G_kn in text). Lower dashed line: linearised Gaussian seamount with $\frac{a\omega}{ND_e}\left(1-\left(\frac{f}{\omega}\right)^2\right)^{1/2} < \frac{1}{\pi}$.

(b) As for (a), but for seamounts with $h_m/a = 0.69$. Here $f/\omega = 0, 0.3, 0.6, 0.8, 0.9, 0.95, 0.99$.

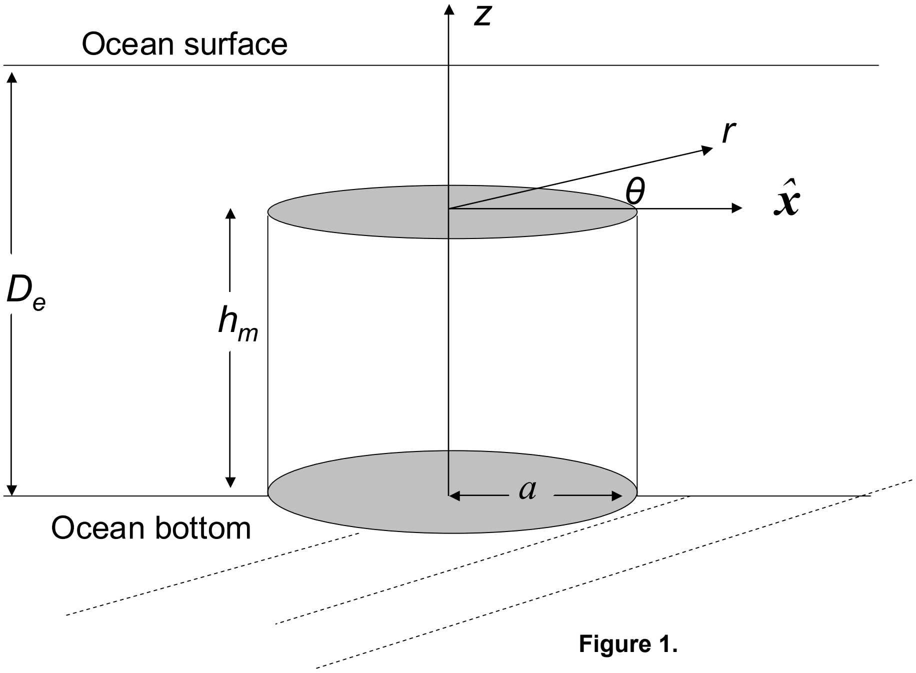

Figure 1.

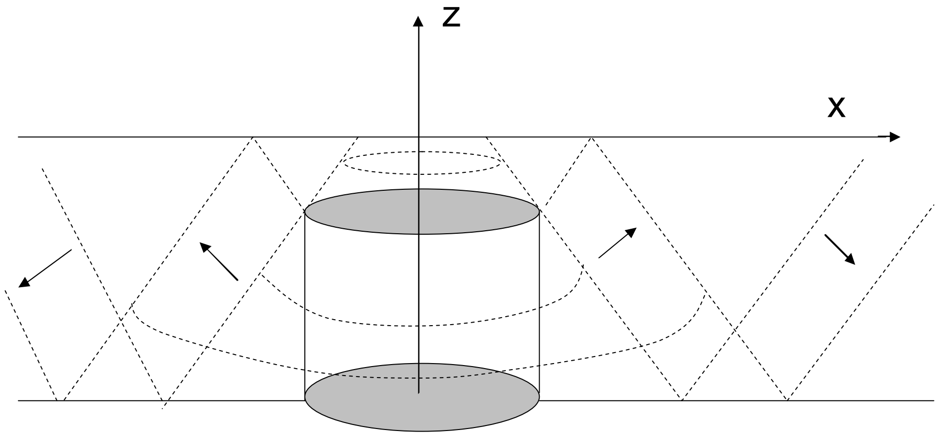

Figure 2.

(a)

Amplitude of radial velocity

$\theta = 0$

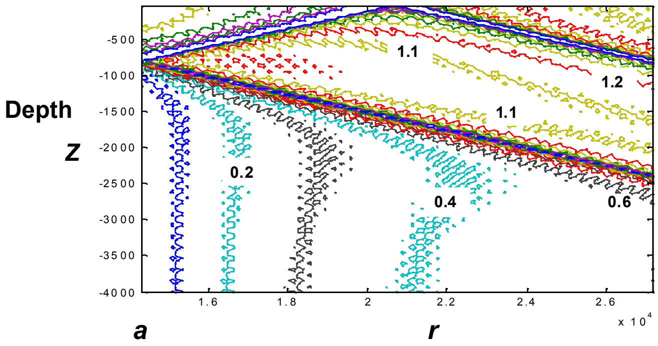

(b)

Phase of radial velocity

$\theta = 0$

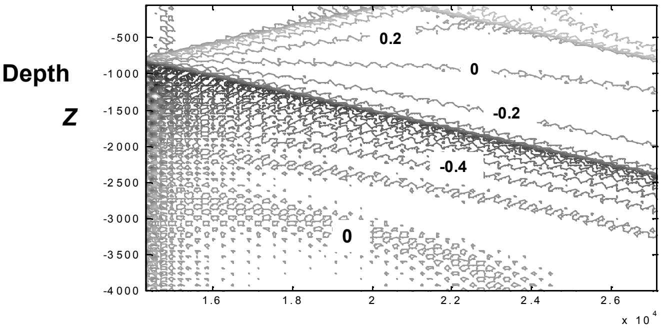

Figure 3

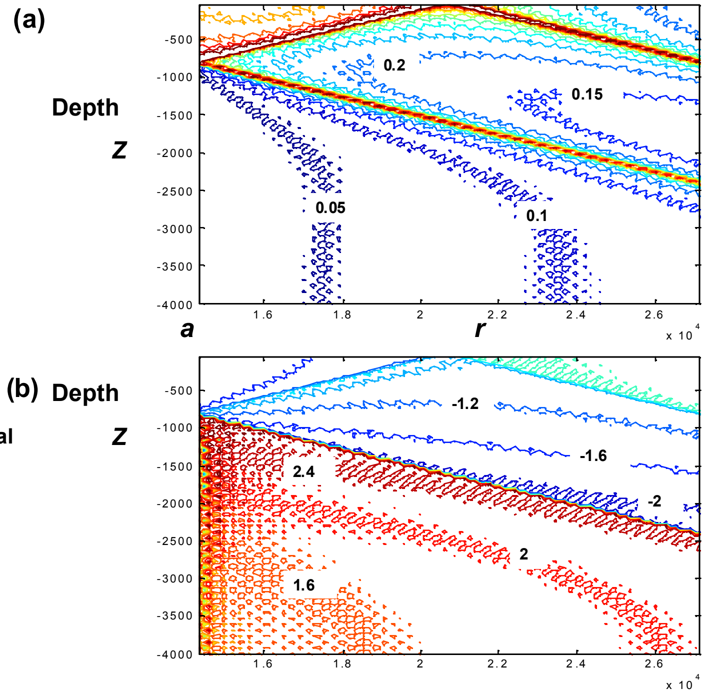

Amplitude of radial velocity

$\theta = \pi/2$

Phase of radial velocity

$\theta = \pi/2$

Figure 4

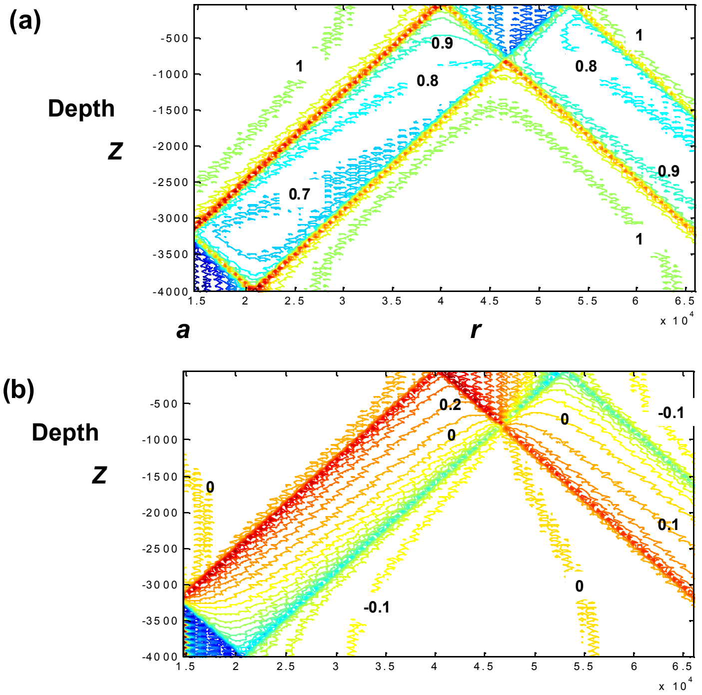

Amplitude of radial velocity

$\theta = 0$

Phase of radial velocity

$\theta = 0$

Figure 5

Figure

Click here to download Figure: Seamounts Fig.6.doc

(a)

Amplitude of radial velocity

θ = π/2

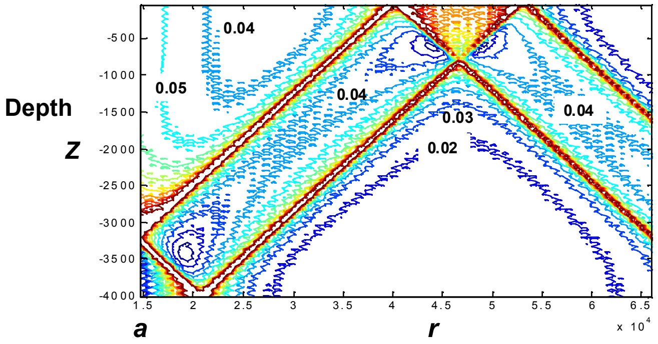

(b)

Phase of radial velocity

θ = π/2

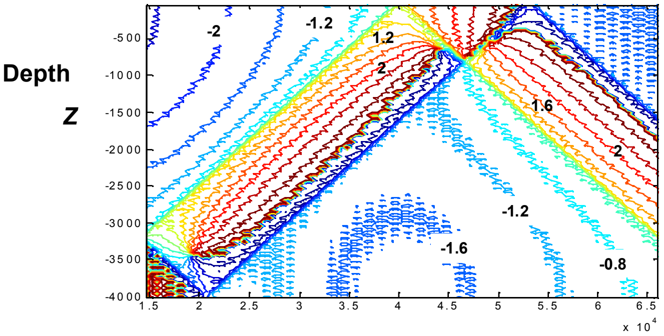

Figure 6

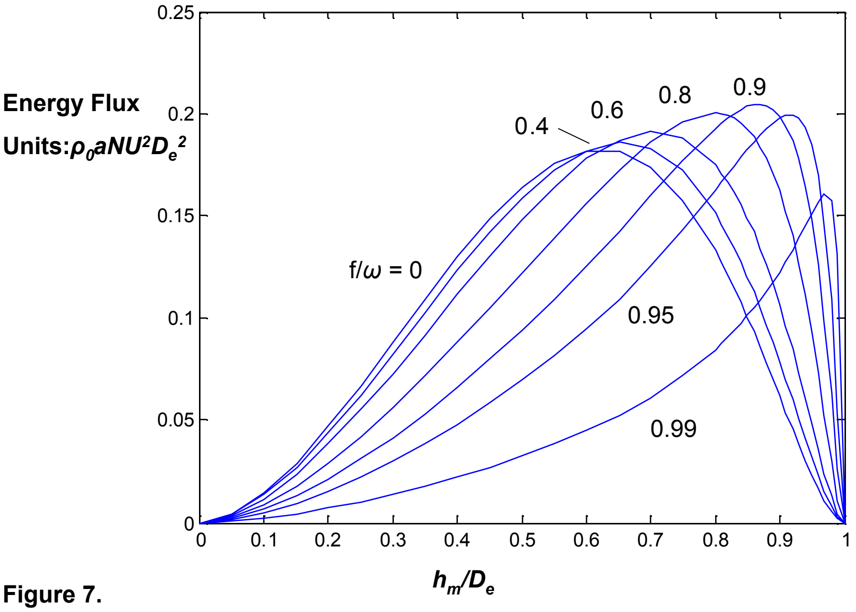
Energy Flux
Units:$\rho_0 a N U^2 D_e^2$
0.25
0.2
0.15
0.1
0.05
0
0
0.1
0.2
0.3
0.4
0.5
0.6
0.7
0.8
0.9
1
h_m/D_e
f/ω = 0
0.4
0.6
0.8
0.9
0.95
0.99

Figure 7.

Figure 8.

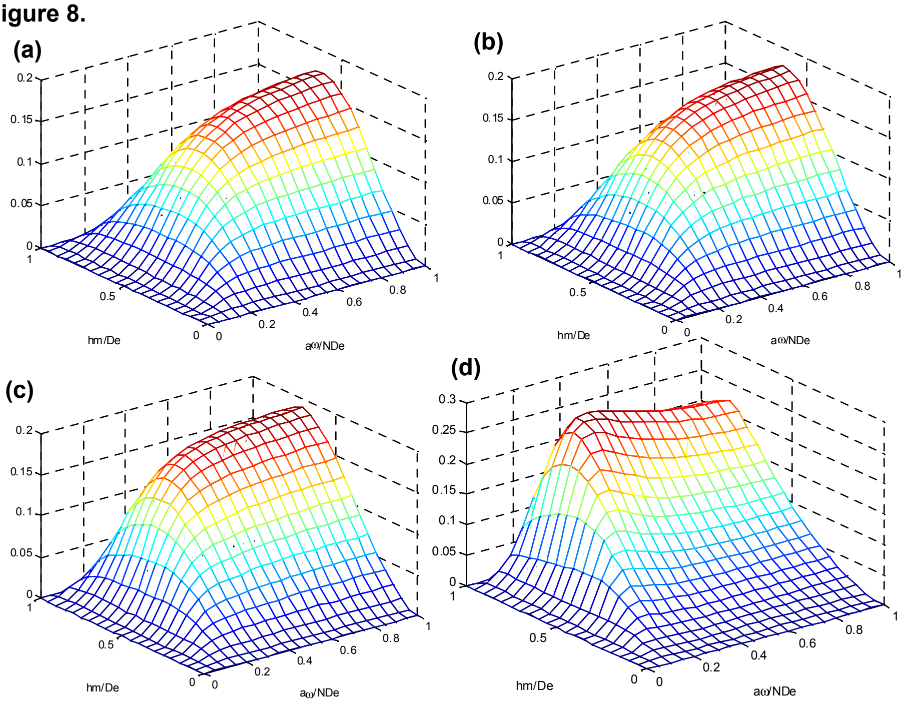

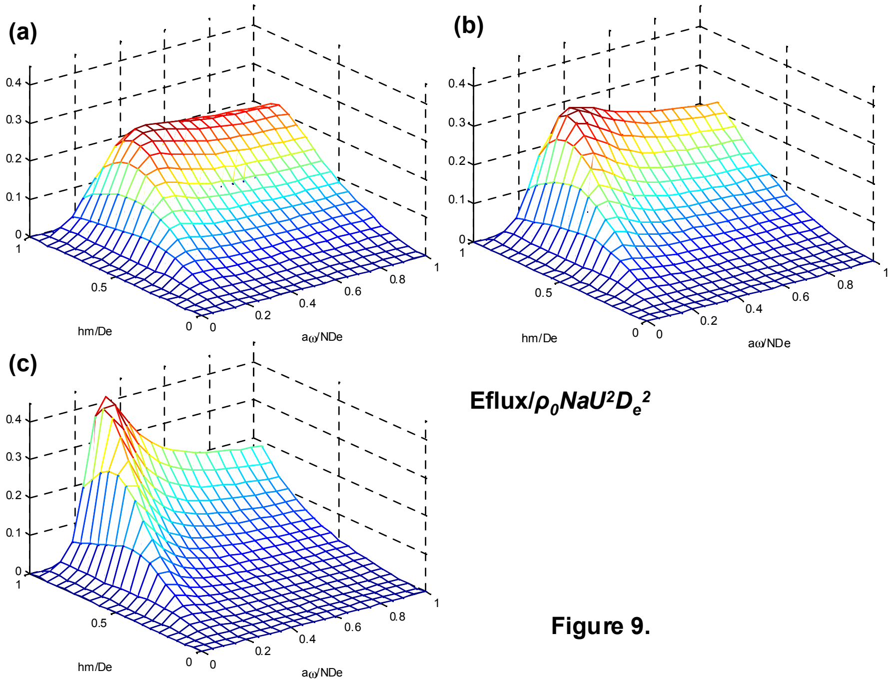
(a)
(b)
(c)
0
0.1
0.2
0.3
0.4
1
0.5
0
hm/De
0
0.2
0.4
0.6
0.8
1
aω/NDe
Eflux/$\rho_0 NaU^2 D_e^2$

Figure 9.

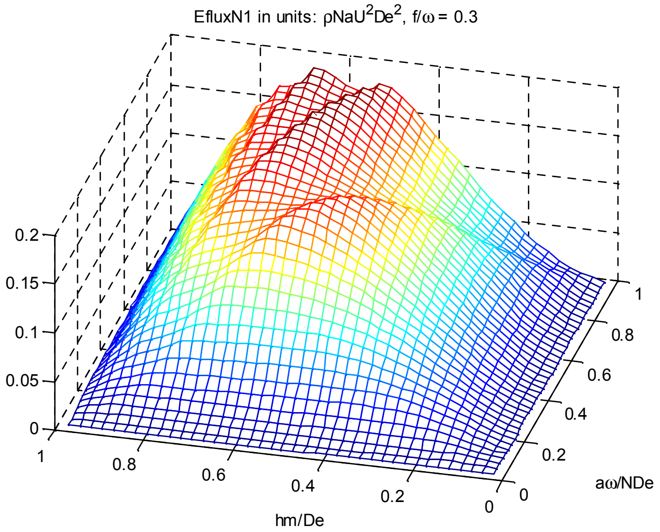
EfluxN1 in units: ρNaU²De², f/ω = 0.3
0.2
0.15
0.1
0.05
0
1
0.8
0.6
0.4
0.2
0
hm/De
1
0.8
0.6
0.4
0.2
0
aω/NDe

Figure 10.

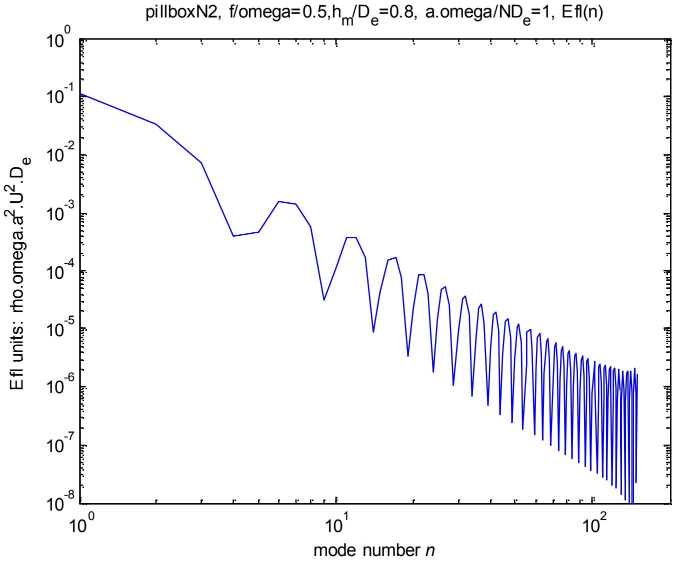
pillboxN2, f/omega=0.5,h$_m$/D$_e$=0.8, a.omega/ND$_e$=1, Efl(n)
Efl units: rho.omega.a^2.U^2.D$_e$
mode number *n*
10^0
10^{-1}
10^{-2}
10^{-3}
10^{-4}
10^{-5}
10^{-6}
10^{-7}
10^{-8}
10^0
10^1
10^2

Figure 11.

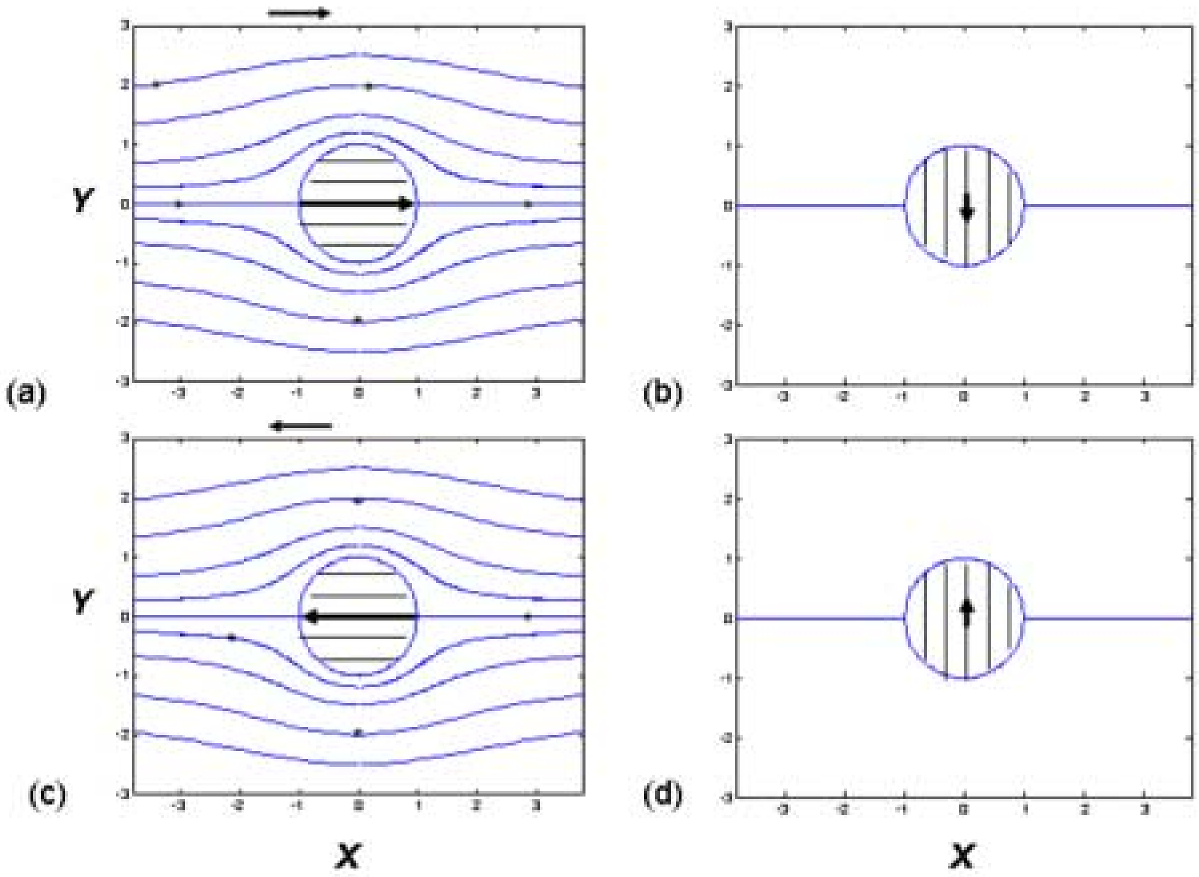

Figure 12

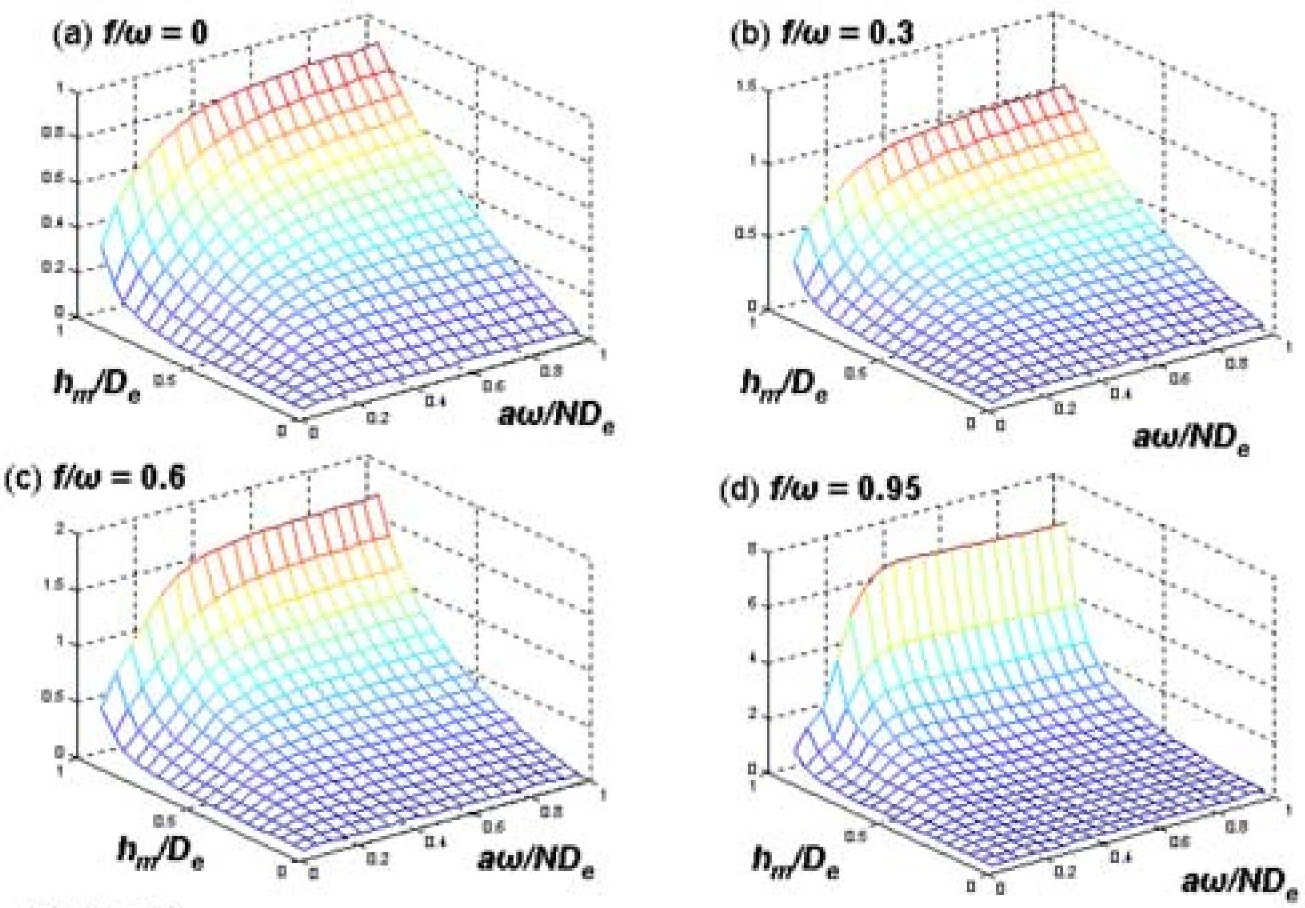
(a) f/ω = 0
0
0.2
0.4
0.6
0.8
1
1
0.5
0
h_m/D_e
0
0.2
0.4
0.6
0.8
1
$a\omega/ND_e$
(b) f/ω = 0.3
0
0.5
1
1.5
1
0.5
0
h_m/D_e
0
0.2
0.4
0.6
0.8
1
$a\omega/ND_e$
(c) f/ω = 0.6
0
0.5
1
1.5
2
1
0.5
0
h_m/D_e
0
0.2
0.4
0.6
0.8
1
$a\omega/ND_e$
(d) f/ω = 0.95
0
2
4
6
8
1
0.5
0
h_m/D_e
0
0.2
0.4
0.6
0.8
1
$a\omega/ND_e$

Figure 13.

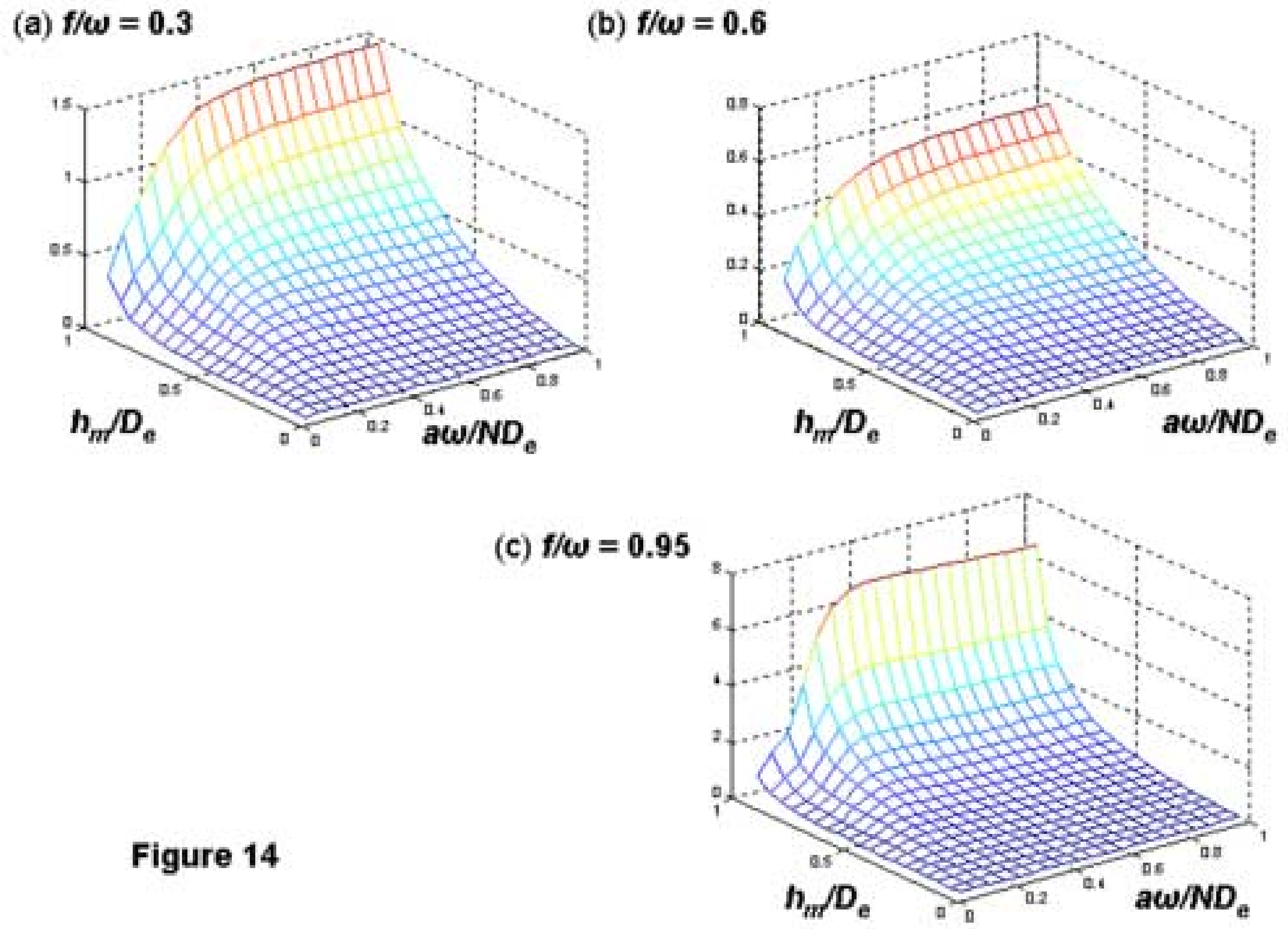
(a) f/ω = 0.3
1.5
1
0.5
0
1
0.5
0
h_m/D_e
0
0.2
0.4
0.6
0.8
1
$a\omega/ND_e$
(b) f/ω = 0.6
0.8
0.6
0.4
0.2
0
1
0.5
0
h_m/D_e
0
0.2
0.4
0.6
0.8
1
$a\omega/ND_e$
(c) f/ω = 0.95
8
6
4
2
0
1
0.5
0
h_m/D_e
0
0.2
0.4
0.6
0.8
1
$a\omega/ND_e$

Figure 14

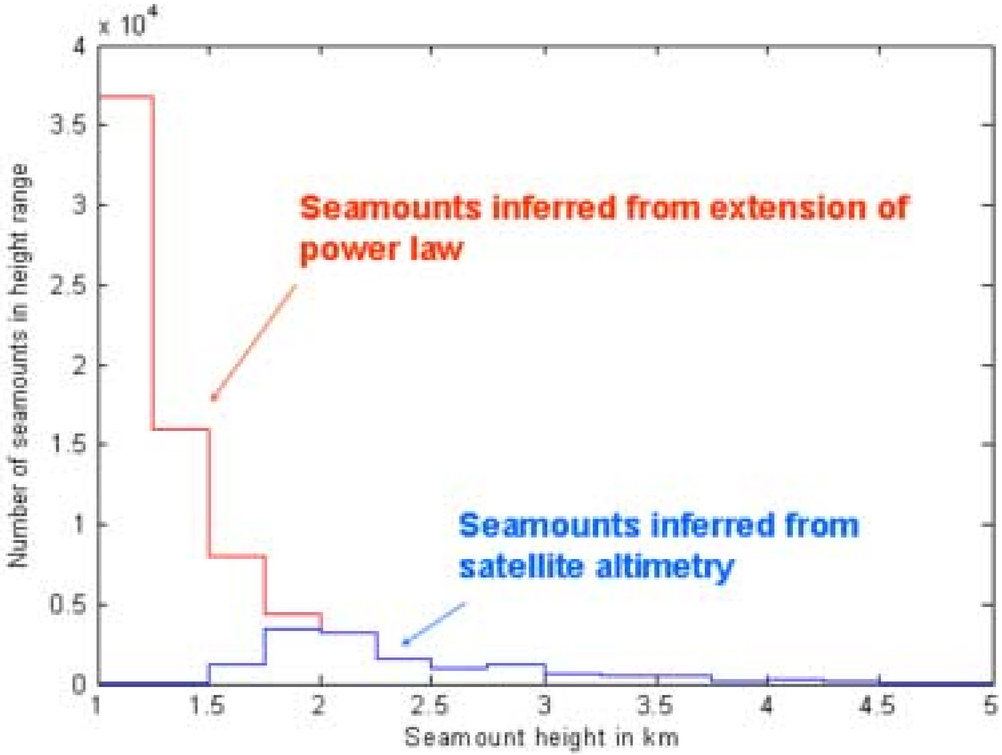
x 10^4
4
3.5
3
2.5
2
1.5
1
0.5
0
Number of seamounts in height range
1
1.5
2
2.5
3
3.5
4
4.5
5
Seamount height in km
Seamounts inferred from extension of power law
Seamounts inferred from satellite altimetry

Figure 15.

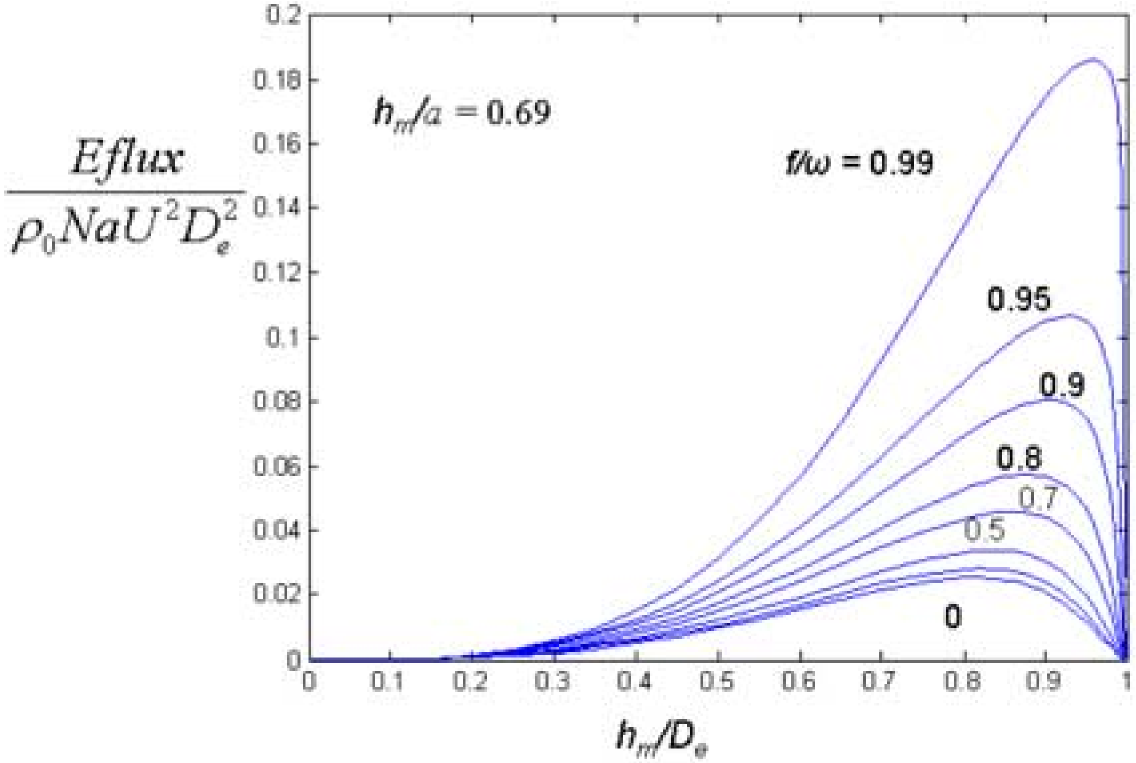
$\frac{Eflux}{\rho_0 NaU^2 D_e^2}$
$h_m/a = 0.69$
$f/\omega = 0.99$
0.95
0.9
0.8
0.7
0.5
0
0.2
0.18
0.16
0.14
0.12
0.1
0.08
0.06
0.04
0.02
0
0
0.1
0.2
0.3
0.4
0.5
0.6
0.7
0.8
0.9
1
h_m/D_e

Figure 16

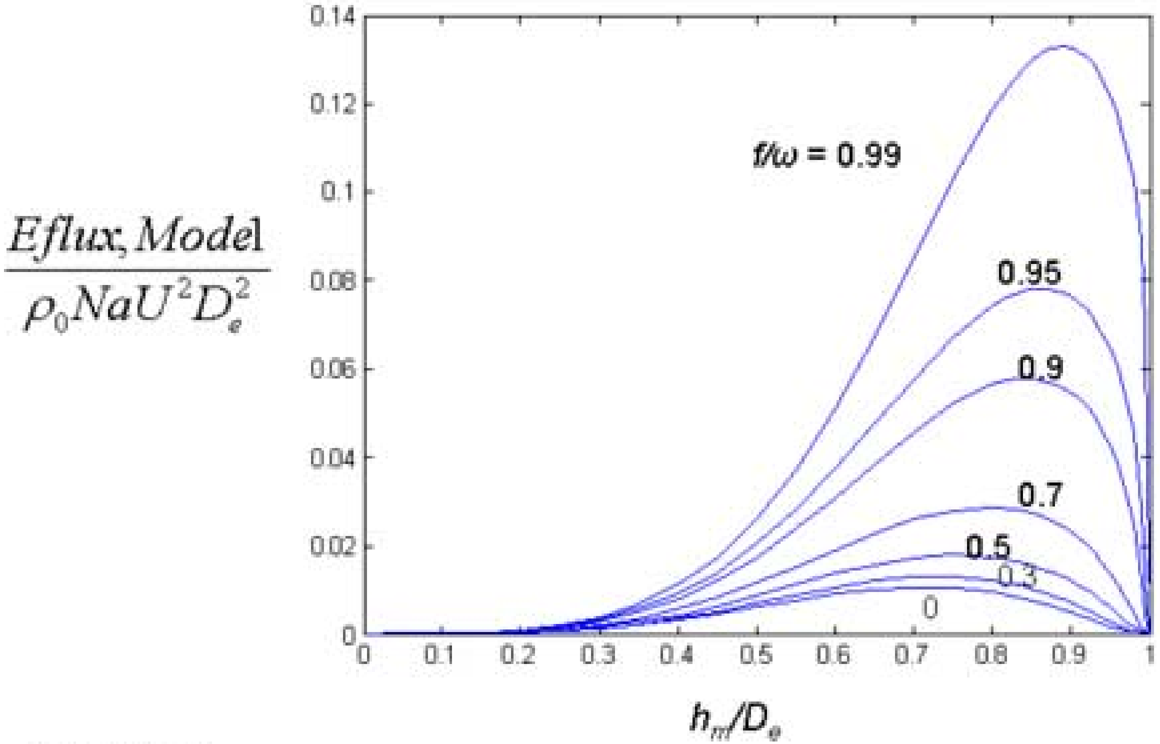
$\frac{Eflux, Model}{\rho_0 N a U^2 D_e^2}$
0.14
0.12
0.1
0.08
0.06
0.04
0.02
0
f/ω = 0.99
0.95
0.9
0.7
0.5
0.3
0
0
0.1
0.2
0.3
0.4
0.5
0.6
0.7
0.8
0.9
1
h_m/D_e

Figure 17a

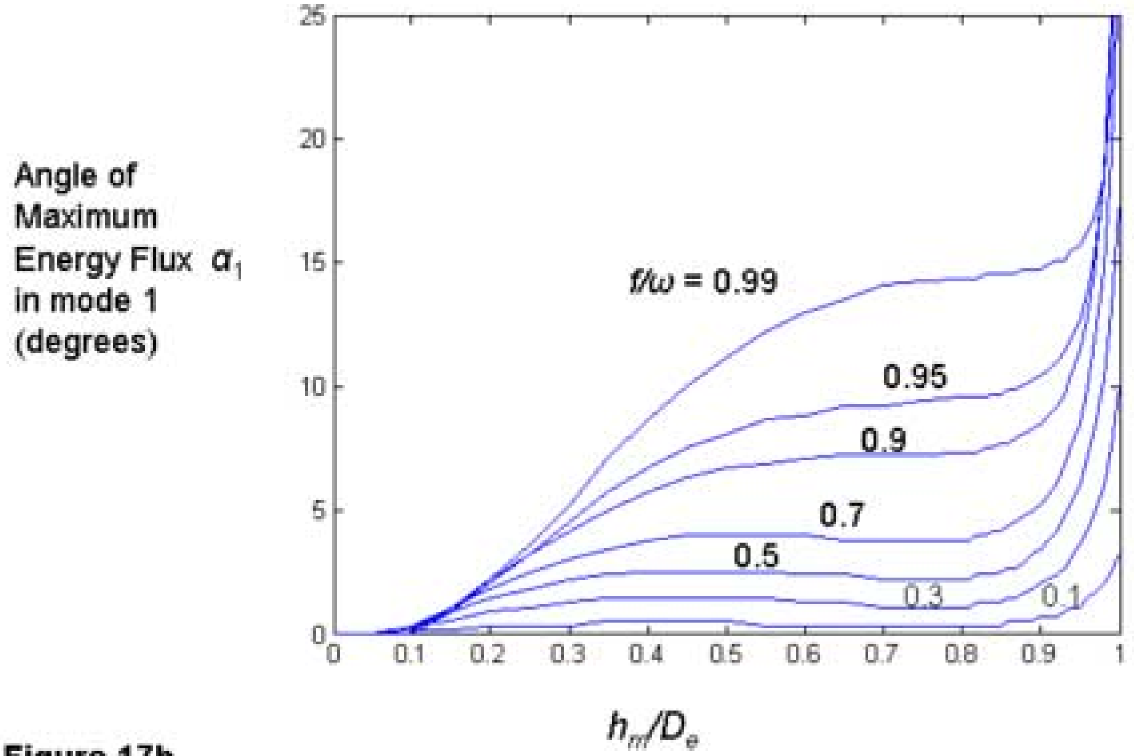
Angle of Maximum Energy Flux α_1 in mode 1 (degrees)
25
20
15
10
5
0
0
0.1
0.2
0.3
0.4
0.5
0.6
0.7
0.8
0.9
1
f/ω = 0.99
0.95
0.9
0.7
0.5
0.3
0.1
h_m/D_e

Figure 17b

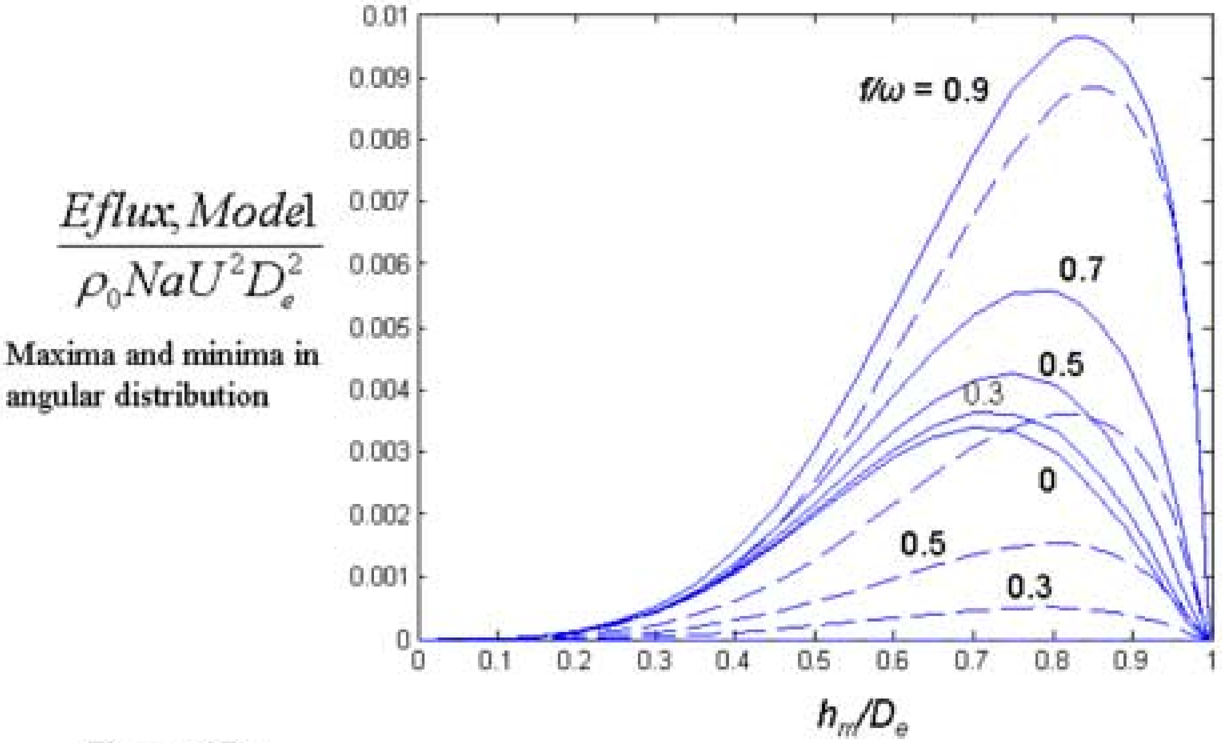
Eflux, Model / $\rho_0 N a U^2 D_e^2$
Maxima and minima in angular distribution
f/ω = 0.9
0.7
0.5
0.3
0
0.5
0.3
0.01
0.009
0.008
0.007
0.006
0.005
0.004
0.003
0.002
0.001
0
0
0.1
0.2
0.3
0.4
0.5
0.6
0.7
0.8
0.9
1
h_m/D_e

Figure 17c

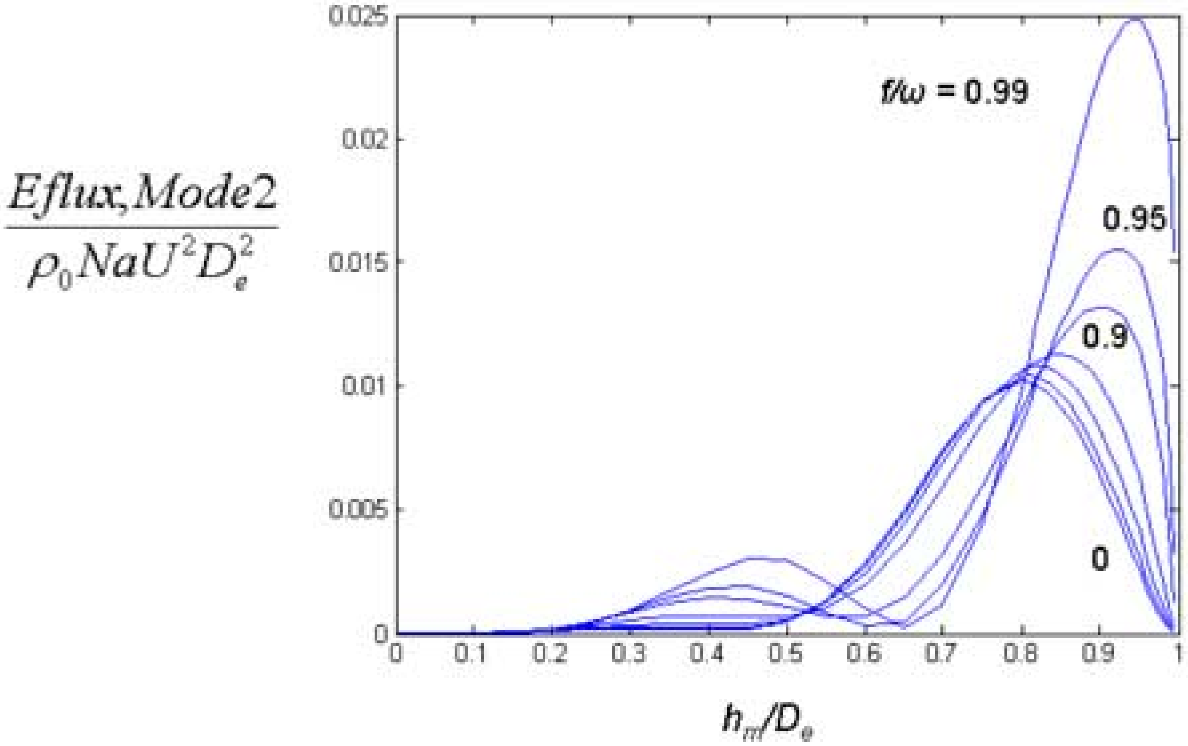
$\frac{Eflux, Mode2}{\rho_0 N a U^2 D_e^2}$
0.025
0.02
0.015
0.01
0.005
0
0
0.1
0.2
0.3
0.4
0.5
0.6
0.7
0.8
0.9
1
f/ω = 0.99
0.95
0.9
0
h_m/D_e

Figure 18a

Angle of
Maximum
Energy Flux α_2
in mode 2
(degrees)

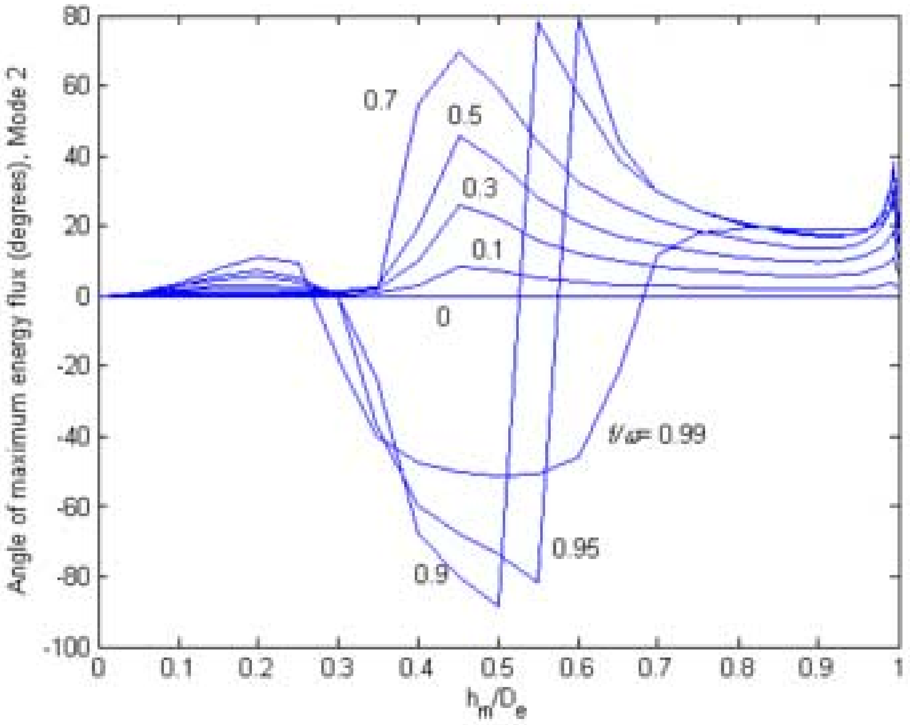

Figure 18b

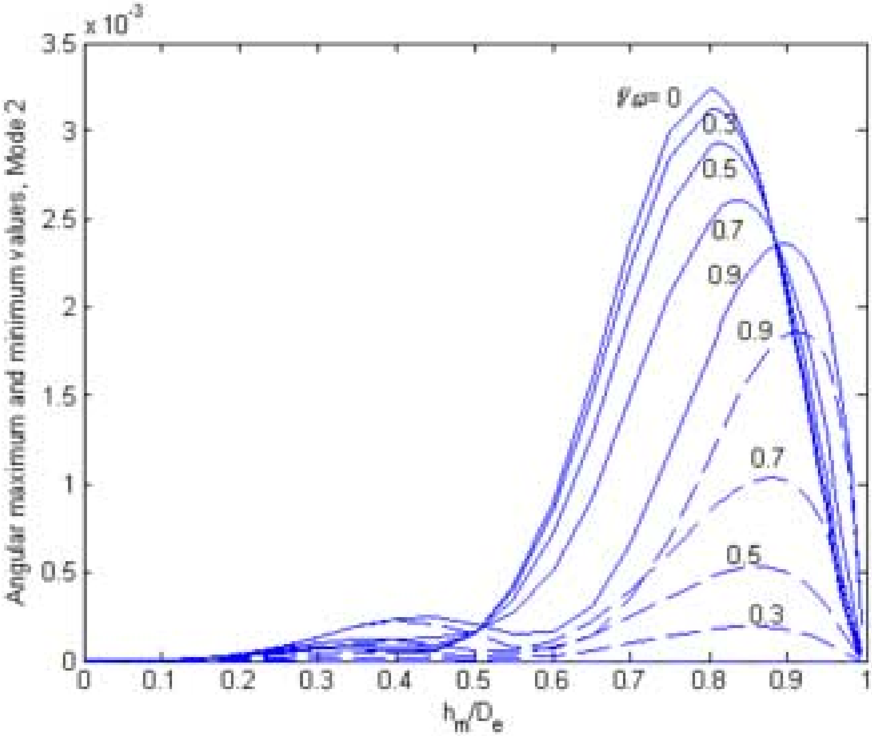
x 10^-3
3.5
3
2.5
2
1.5
1
0.5
0
Angular maximum and minimum values, Mode 2
γω= 0
0.3
0.5
0.7
0.9
0.9
0.7
0.5
0.3
0
0.1
0.2
0.3
0.4
0.5
0.6
0.7
0.8
0.9
1
h_m/D_e

Figure 18c

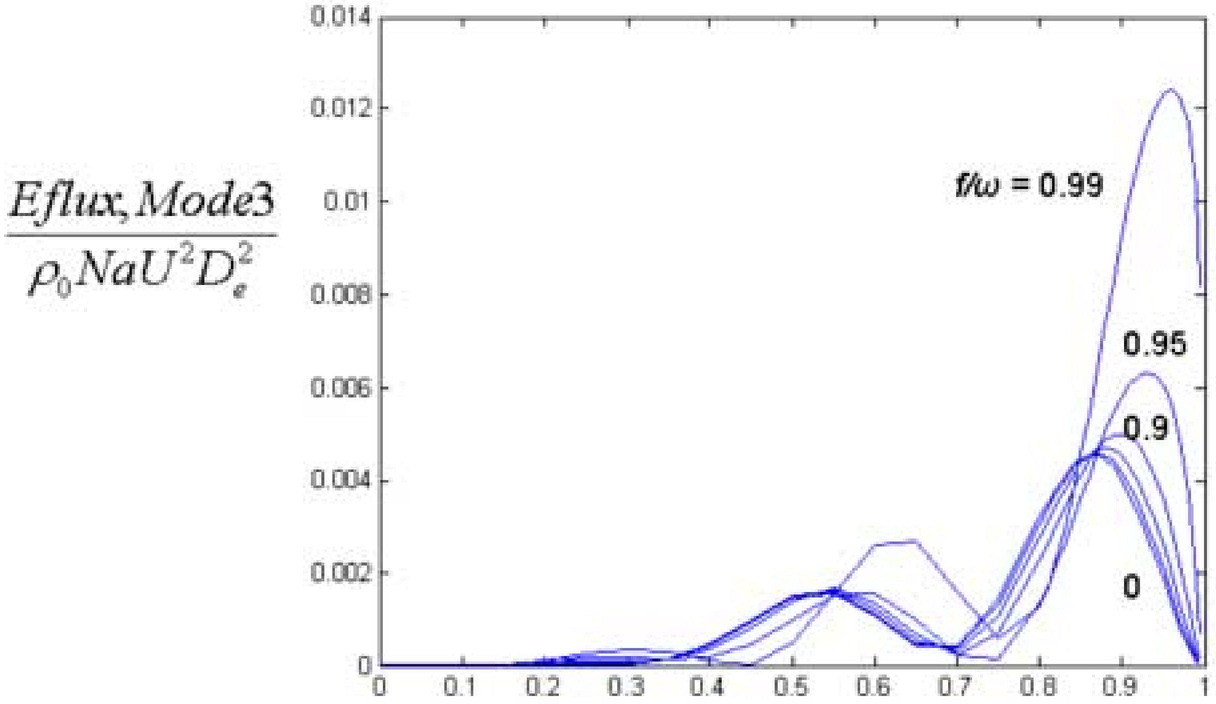
Eflux, Mode3 / ρ0 N a U2 De2
0.014
0.012
0.01
0.008
0.006
0.004
0.002
0
0
0.1
0.2
0.3
0.4
0.5
0.6
0.7
0.8
0.9
1
f/ω = 0.99
0.95
0.9
0

Figure 19a

Angle of
Maximum
Energy Flux α_3
in mode 3
(degrees)

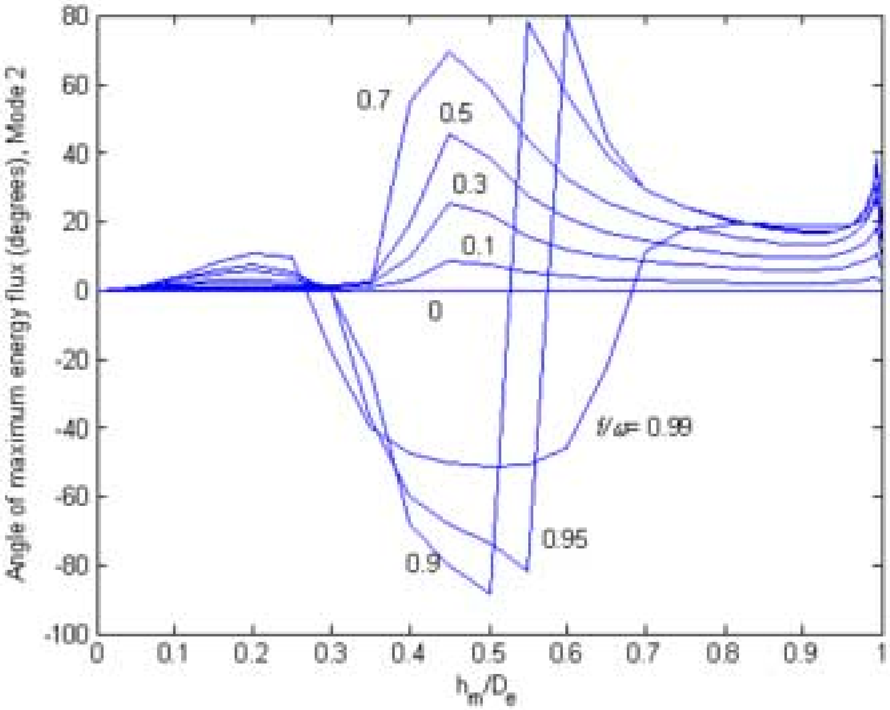

Figure 19b

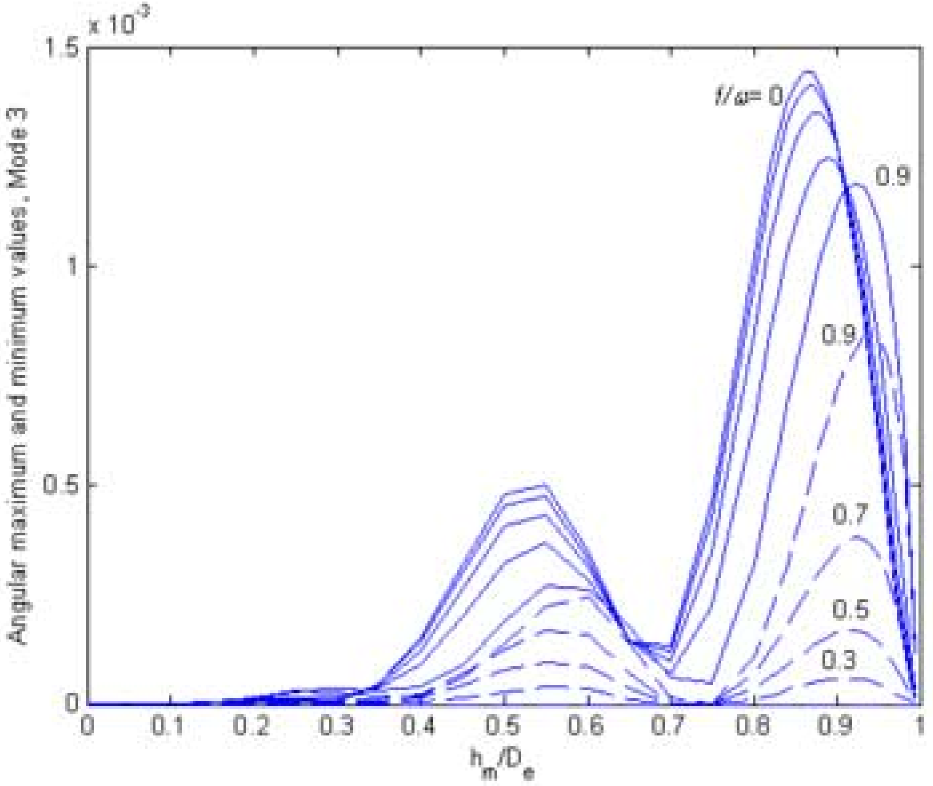
x 10^-3
1.5
1
0.5
0
0
0.1
0.2
0.3
0.4
0.5
0.6
0.7
0.8
0.9
1
Angular maximum and minimum values, Mode 3
h_m/D_e
f/ω= 0
0.9
0.9
0.7
0.5
0.3

Figure 19c

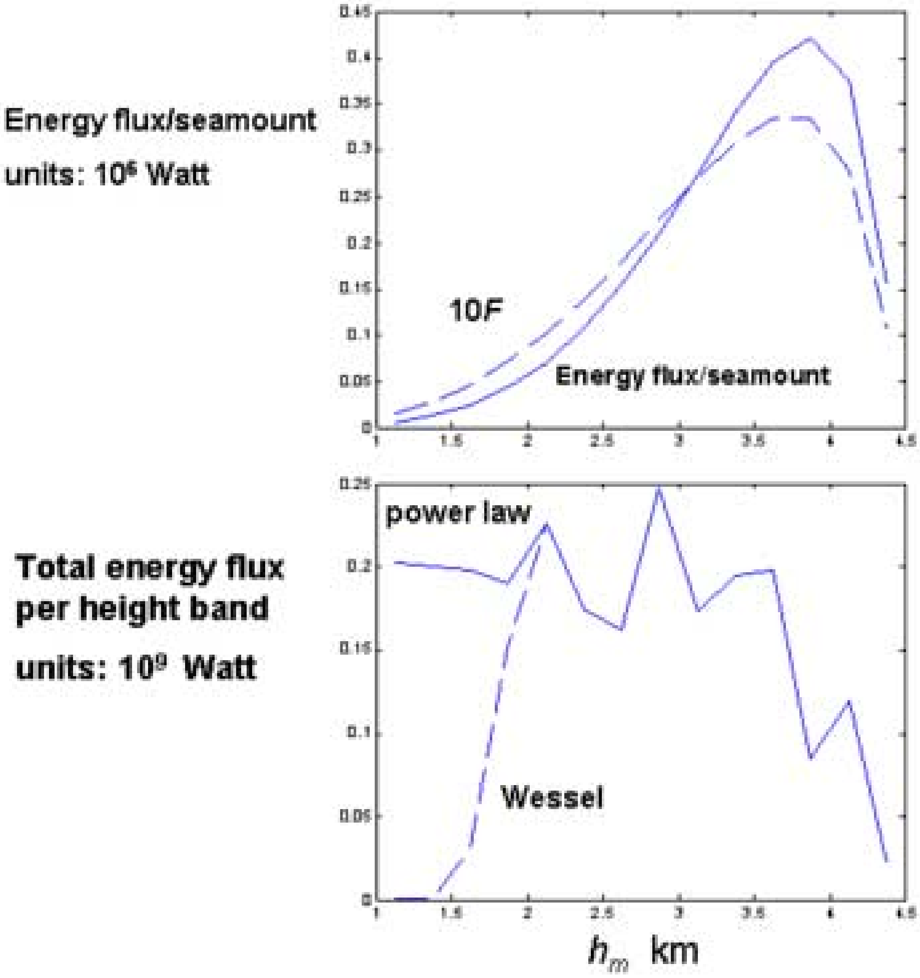
Energy flux/seamount
units: 10^6 Watt
0.45
0.4
0.35
0.3
0.25
0.2
0.15
0.1
0.05
0
10F
Energy flux/seamount
1
1.5
2
2.5
3
3.5
4
4.5
Total energy flux
per height band
units: 10^9 Watt
0.25
0.2
0.15
0.1
0.05
0
power law
Wessel
1
1.5
2
2.5
3
3.5
4
4.5
h_m km

Figure 20.

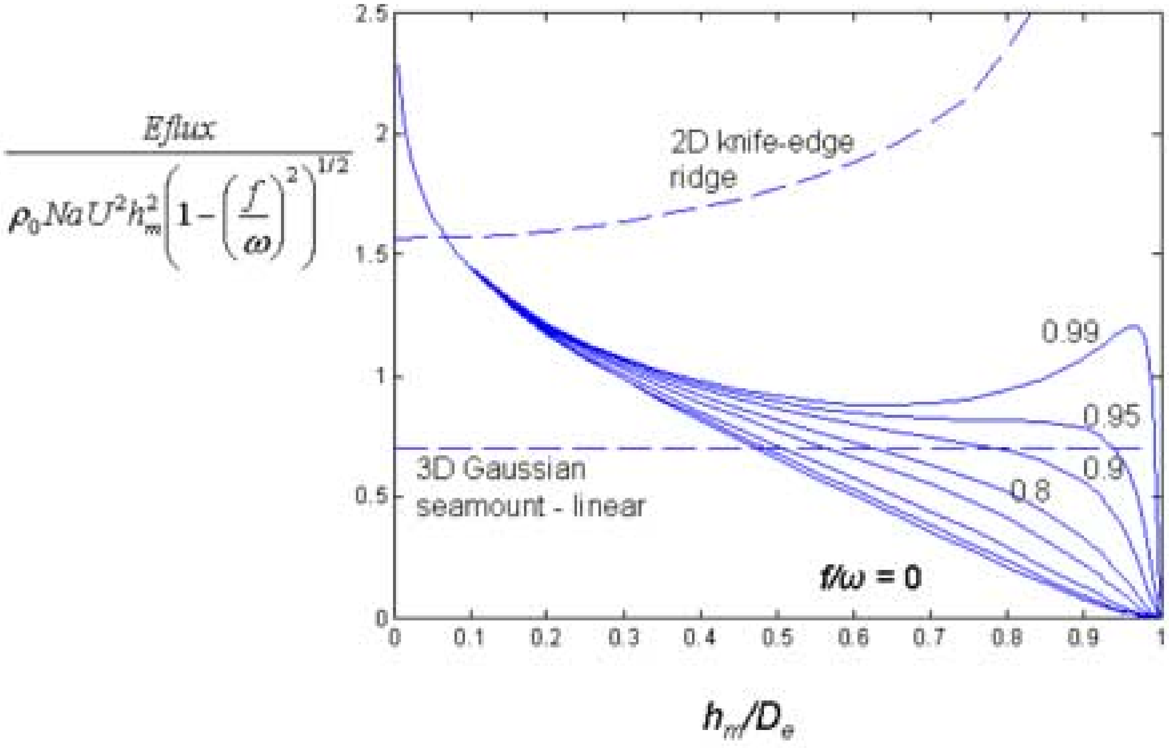
$\frac{Eflux}{\rho_0 N a U^2 h_m^2 \left(1-\left(\frac{f}{\omega}\right)^2\right)^{1/2}}$
2.5
2
1.5
1
0.5
0
0
0.1
0.2
0.3
0.4
0.5
0.6
0.7
0.8
0.9
1
2D knife-edge ridge
3D Gaussian seamount - linear
0.99
0.95
0.9
0.8
$f/\omega = 0$
h_m/D_e

Figure 21a

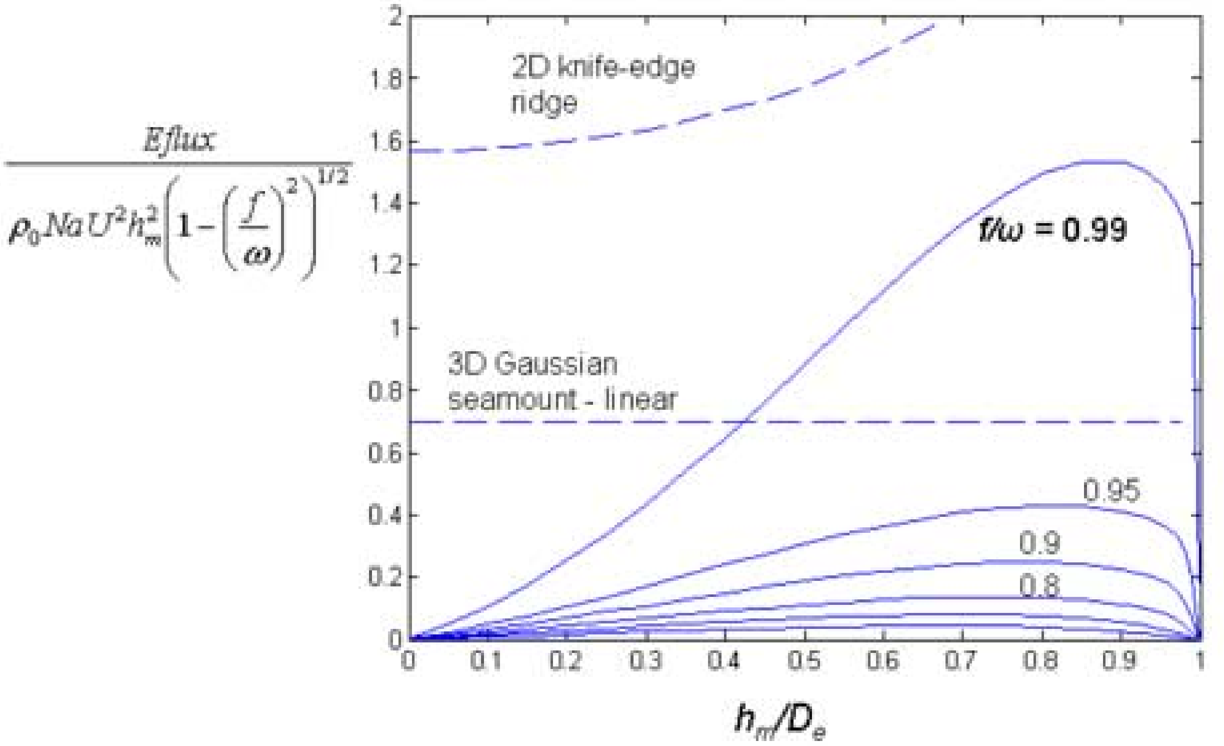
$\frac{Eflux}{\rho_0 Na U^2 h_m^2 \left(1-\left(\frac{f}{\omega}\right)^2\right)^{1/2}}$
2D knife-edge ridge
f/ω = 0.99
3D Gaussian seamount - linear
0.95
0.9
0.8
0
0.2
0.4
0.6
0.8
1
1.2
1.4
1.6
1.8
2
0
0.1
0.2
0.3
0.4
0.5
0.6
0.7
0.8
0.9
1
h_m/D_e

Figure 21b

Reply to Reviewer 1

I am grateful to the reviewer for his careful reading of the manuscript, and his constructive comments. The paper has been substantially revised, and all of his major suggestions have been acted upon. The substance of the original version is unchanged, but additional material that includes a new section on comparison with other models and more figures showing the character of the three-dimensional flow field (specifically Figures 17-19) have been included. An x-y cross section of the barotropic part of the flow has also been added.

Reply to Reviewer 2

I am grateful to the reviewer for his interest in the manuscript and his careful reading of it, his attention to the details, and his constructive comments which have led to substantial improvements. His comments are too numerous for a detailed response to all of them, but all of his major suggestions have been acted upon, and most of the minor ones. The substance of the original version is unchanged, but additional material that includes a new section on comparison with other models and more figures showing the character of the three-dimensional flow field (specifically Figures 17-19) have been included. More information on the barotropic flow has been included, including an x-y cross section of it (Figure 12).

Some specifics:

I have retained the subscripts to h_m and D_e because h is often a function for the shape, and there are other Ds in the paper.

Plan views of flow patterns have been avoided – too complex and too many options (which depths, which phases, which parameter values etc.?). Figures 17-19 are a good alternative, I believe.

The variable stratification paragraphs are retained. The stratification is quite realistic, being the response to mechanical stirring of uniform stratification (by wind) at the surface. No figures are involved.